

# Measurement of aspherical mirrors with PMD

**Masterarbeit aus der Physik**

Vorgelegt von  
**Andreas Specovius**  
am 2.11.2016

Erstellt am  
Erlangen Centre for Astroparticle Physics (ECAP)  
Friedrich-Alexander-Universität Erlangen-Nürnberg



Erstgutachter: Prof. Dr. Christopher van Eldik  
Zweitgutachterin: Prof. Dr. Gisela Anton

## Abstract

The next generation gamma ray telescope Cherenkov Telescope Array (CTA) will consist partly of several two-mirrored imaging atmospheric cherenkov telescopes. The optical system of these so called Schwarzschild-Couder Telescopes (SCT) makes use of aspherical mirrors. In order to ensure a high operation quality of the telescope its single mirror facets have to be of a sufficiently high quality. Currently, no quality testing procedures are available for aspherical mirrors.

The aim of this thesis is to adapt an existing mirror characterization and measurement procedure for spherical telescope mirrors to aspherical mirror facets of the SCT design. It is made use of the mirror measuring technique *phase measuring deflectometry* (PMD, Wörnlein 2012), which is the approved method for measuring CTAs spherical telescope mirrors. Modifications to the existing evaluation approach and a further definition of the mirror characterization parameters are developed.

In the modified evaluation approach, the point spread function (PSF) of an aspherical mirror facet is described by an ellipse with two diameters  $u$  and  $v$ . To characterize the mirror quality, the curvature radii of the mirror are determined and the mirrors surface height and slope deviation is analyzed.

Ideal and real versions of one type of the aspherical mirror facets needed in the SCT are measured and evaluated in that way. Using the modified evaluation approach the curvature radii are measurable up to an accuracy of below 0.5 %.

In order to further improve the measurement quality of aspherical mirrors, a new evaluation approach was introduced which describes the mirror surface as a rotationally symmetric prolate ellipsoid. The results are compared to the modified existing approach. The potential of that new evaluation approach seems to be promising.

# Contents

<b>List of abbreviations</b>	<b>iv</b>
<b>1 Introduction to CTA and the Schwarzschild-Couder Telescope</b>	<b>1</b>
<b>2 Phase measuring deflectometry</b>	<b>6</b>
2.1 From patterns to slopes . . . . .	6
2.2 From slopes to the point spread function . . . . .	10
<b>3 The Schwarzschild–Couder Telescope</b>	<b>11</b>
3.1 Telescope design . . . . .	11
3.2 Mirror segmentation . . . . .	12
3.3 Mathematical mirror description . . . . .	12
3.4 Curvature and focal planes . . . . .	15
3.5 Comparison of aspheres and spheres . . . . .	18
<b>4 Simulating aspherical mirror facets</b>	<b>20</b>
4.1 Introduction to simulating PMD measurements . . . . .	20
4.2 Integration of aspherical mirrors in PMD simulations . . . . .	21
<b>5 Measuring ideal aspherical mirror facets with a spherical surface model</b>	<b>28</b>
5.1 Image merging quality . . . . .	28
5.2 Determination of curvature radii and the importance of mirror orientation . . . . .	31
5.3 Other methods of mirror quality analysis . . . . .	38
5.3.1 Surface reconstruction . . . . .	38
5.3.2 Height deviation . . . . .	39
5.3.3 Slope deviation . . . . .	41
5.4 Discussion and conclusion . . . . .	42
<b>6 Application to the mirror facet P1.016 from the prototype Schwarzschild–Couder Telescope</b>	<b>46</b>
6.1 Determination of curvature radii and focal planes . . . . .	46
6.1.1 2f measurement . . . . .	46
6.1.2 PMD measurement . . . . .	48
6.2 Height deviation . . . . .	49
6.3 Slope deviation . . . . .	49
6.4 Conclusion . . . . .	50

<b>7</b>	<b>Measuring aspherical mirror facets with an ellipsoidal surface model</b>	<b>53</b>
7.1	Curvature Radii of the ideal aspherical mirror . . . . .	54
7.2	Curvature Radii of the real aspherical mirror . . . . .	54
7.3	Height deviation . . . . .	57
7.4	Slope deviation . . . . .	57
7.5	Discussion and conclusion . . . . .	60
<b>8</b>	<b>Summary and Outlook</b>	<b>63</b>
	<b>Appendix</b>	<b>65</b>
	<b>Bibliography</b>	<b>66</b>
	<b>Acknowledgment</b>	<b>68</b>
	<b>Statement of authorship</b>	<b>69</b>



## List of abbreviations

**ATLAS** a toroidal LHC apparatus

**CERN** Conseil Européen pour la Recherche Nucléaire

**CTA** Cherenkov Telescope Array

**DC** Davies-Cotton

**PMD** Phase Measuring Deflectometry

**FOV** field of view

**H.E.S.S.** High Energy Stereoscopic System

**IACT** imaging atmospheric cherenkov telescope

**LHC** Large Hadron Collider

**LST** large sized telescope

**MST** medium sized telescope

**P1** mirror facet of the inner ring of the primary mirror dish

**PS** point spread

**PSF** point spread function

**SC** Schwarzschild–Couder

**SCT** Schwarzschild–Couder Telescope

**SST** small sized telescope

**UA1** Underground Area 1

# 1 Introduction to CTA and the Schwarzschild-Couder Telescope

Most of the fundamental results in the field of research of particle physics such as the discovery of the W- and Z-bosons (UA1 Collaboration 1983) or the verification of the Higgs mechanism (ATLAS Collaboration 2012) was made possible by large hadron colliders like today's LHC at CERN (see Evans & Bryant 2008). With its design center of mass energy of 14 TeV it is the strongest particle collider existing on earth. Currently, plans come up with new and stronger accelerators in order to answer still open questions in today's physics, but this trend will be limited by cost, resources and space.

While discussions about building the next generation particle accelerator are still underway, every second highly-energetic particles and photons, so-called gamma rays, collide with the atmosphere above our heads. Cosmic rays were discovered by Victor Franz Hess who finally was awarded in 1936 with the Nobel Prize of physics for his work. With his discovery he opened a new field of research, the astroparticle physics. Since then, the examination of the sources of highly-energetic cosmic rays has been put on another level of importance. The universe contains a variety of potential source candidates that accelerate charged particles, mainly hydrogen and helium nuclei. But, as these particles are electrically charged, they are deflected by cosmic magnetic fields while traveling through the universe on their way to the earth. Hence, the amount of information that can be obtained about their source is limited. These source candidates accelerating charged particles are also predicted to emit gamma rays as a by-product. In contrast to charged particles, gamma rays travel in straight lines and therefore allow an identification of their source point (see Helmholtz Association 2016).

The investigation of the sources of highly-energetic gamma rays has been pushed forward in the last decade. There are observatories such as Fermi located in space or the imaging atmospheric cherenkov telescope (IACT) H.E.S.S. located on earth which examine this radiation. As the flux of gamma rays decreases for higher energies, the detection of the very-high-energy gamma rays with energies above a few hundred GeV with a satellite is difficult. A huge detection area in the satellite would be needed in order to detect just a few of them which would make them prohibitively expensive.

The great advantage of ground based observatories like H.E.S.S. compared to spaceborne observatories is, that the atmosphere works as an active medium for the detectors which enlarges their effective area a lot. The gamma rays interact with the atmosphere and produce air showers of secondary particles. These secondary particles are highly energetic and move faster than the speed of light in the surrounding medium. Due to that cherenkov radiation is

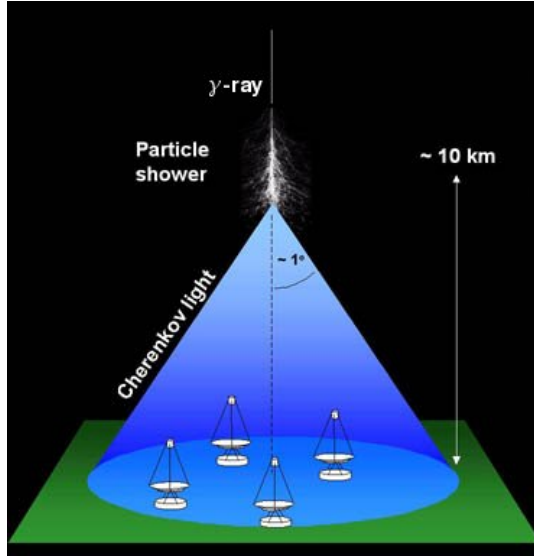


Figure 1.1: The very high energy gamma ray interacts with the atmosphere and creates an air shower of secondary particles. Those are highly energetic and move faster than the speed of light in the surrounding medium. The emitted cherenkov light can be detected on earth (Image from Durham University 2015).

emitted, which manifests as a bluish light, and can be detected on earth. The cherenkov light cone is directly connected to the originating gamma ray energy and its direction. In order to be able to reconstruct these parameters the air shower has to be resolved spatially. This can be done via a stereoscopic measurement setup like in H.E.S.S. Figure 1.1 illustrates the way how highly-energetic gamma rays interact with the atmosphere and how they can finally be detected (Durham University 2015).

One of the next generation ground based gamma ray observatory will be the Cherenkov Telescope Array (CTA) (see Hinton et al. 2013). With the help of this instrument scientists hope to answer open questions concerning cosmic rays, dark matter and the violation of the Lorentz Invariance. With its innovative three sized telescope approach it will be 5 to 10 times more sensitive than today's cherenkov telescopes and will expand the covered energy range from below 100 GeV up to 100 TeV (see figure 1.2, Achary et al. 2013). CTA will most probably be hosted on the European Southern Observatory (ESO) Paranal grounds in Chile and at the Instituto de Astrofísica de Canarias (IAC), Roque de los Muchachos Observatory in La Palma, Spain (Consortium 2016). The southern site is less than 10 km southeast of ESO's existing Paranal Observatory in the Atacama Desert, which is considered one of the driest and most isolated regions on earth and therefore ideal for astronomical observatories.

CTA will consist of a small number of large sized telescopes (LSTs) for the lowest energies  $\leq 100$  GeV with a diameter of 24 m and a field of view (FOV) of 4–5 degrees, several medium

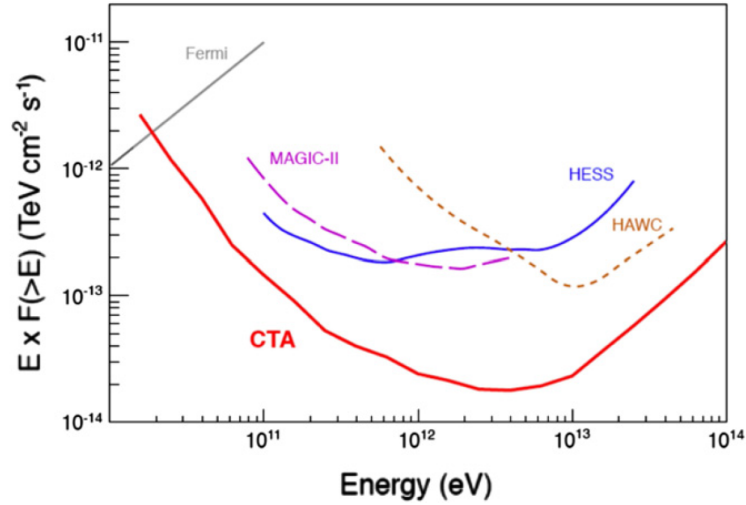


Figure 1.2: Integral sensitivity for CTA from Monte Carlo simulations, compared to other gamma ray observatories in comparable conditions (50 h for IACTs, 1 year for Fermi–LAT and HAWC) (figure from Achary et al. 2013).

sized telescopes (MSTs) for the mediate energies 0.1–10 TeV with a diameter of 12 m and a FOV of 6–8 degrees and lots of small sized telescopes (SSTs) for the highest energies >10 TeV with a diameter of about 6 m and a FOV of about 10 degrees depending on the actual telescope design. The LSTs will be built in the traditional Davies–Cotton (DC) design. For the MSTs and SSTs prototypes have already been built for DC and Schwarzschild–Coudé designs (see figure 1.3 for comparison, Achary et al. 2013). The first telescopes to be built on the site are planned for 2017.

The traditional single mirror telescopes<sup>1</sup> are dominated by the cost of the cherenkov camera which consists of numerous photo–multipliers composing a large focal plane area. Hence single–mirror telescope designs are not ideal for covering a wide field of view. An alternative approach is given by the Schwarzschild–Coudé (SC) telescope design. Its aplanatic two–mirrored nature is capable of covering a wide FOV while providing an improved angular resolution compared to the Davies–Cotton design. Furthermore the SC optical design corrects for spherical and comatic aberrations (Byrum et al. 2015). It is planned to complete the telescope setup of CTA by equipping some of the MSTs and SSTs with the SC design. SC telescopes are currently developed for CTA.

To ensure a high operation quality and efficiency of every single telescope within CTA it is important to use high quality optical mirrors which reflect the incoming light to the telescope camera. High mirror quality ensures the capability of focusing light in one pixel of the telescope camera. For spherical mirrors as used in the DC telescopes, testing procedures as

<sup>1</sup>Davies–Cotton (DC) or paraboloidal designs are referred to as the traditional telescope designs.

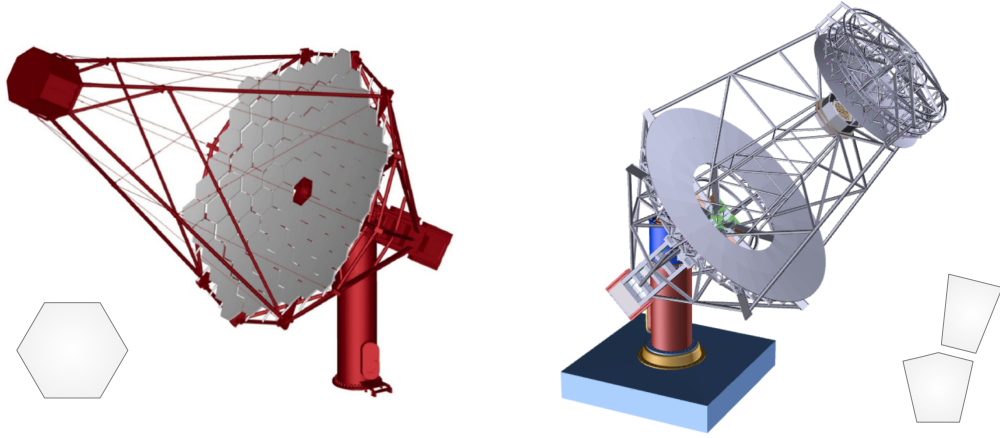


Figure 1.3: Illustration of the IACT designs Davies Cotton (left) and Schwarzschild–Couder (right) for MSTs. The two mirrored nature of the SCT design is visible (Images from Achary et al. 2013; Vandenbroucke 2014). The shape of the single mirror facets is sketched.

well as quality constraints on the mirrors are existing. In contrast, for aspherical mirrors used in the SC telescopes they are not. For spherical mirrors, the quality requirement specifies that per mirror at least 80 % of the reflected light at the plane of the telescope camera has to be contained within a circle of a diameter that corresponds to  $\frac{2}{3}$  of the diameter of a single camera pixel. The quality requirement is on the point spread function<sup>2</sup> (PSF) describing the reflection characteristic of the mirror and not on its surface condition. The 80 % containment diameter is called d80 and is used to characterize the mirrors PSF. In contrast it is point less to adapt the same parameter to single mirrors used in the SC telescopes as the PSF of those aspherical mirrors can not adequately be described by a circle.

The aim of this thesis is to adopt the existing mirror characterization and measurement procedures of spherical telescope mirrors to aspherical mirrors for the SCT. This includes modifications to the existing evaluation approach as well as further definition of the mirror characterization parameters. A new approach for evaluating aspherical mirrors is implemented and compared to the modified existing approach. It is made use of the mirror measuring technique *phase measuring deflectometry* (PMD, Wörnlein 2012), which is the approved method for measuring CTAs spherical telescope mirrors.

The structure of this thesis is as follows: In chapter 2 a short introduction to the mirror measurement technique phase measuring deflectometry is given. Illustrated are the steps that have to be taken in order to determine the mirrors point spread function based on PMD. Chapter 3 describes the Schwarzschild–Couder telescope design in detail and offers the surface description of its mirrors. In chapter 4 it is explained how aspherical mirror facets

<sup>2</sup>The point spread function can be understood as the spatially resolved transfer function of the imaging system.

can be simulated in the context of PMD and in chapter 5 the PMD evaluation is applied to these simulations in order to study systematics. It is shown which modifications to the existing evaluation procedure for spherical mirrors were developed and which results can be achieved. In chapter 6 the modified evaluation technique is applied to a real aspherical SCT mirror. Chapter 7 offers a new approach for evaluating aspherical telescope mirrors and compares it to the modified existing evaluation approach. Chapter 8 summarizes the content of this thesis and provides an outlook on how the obtained results are referable in the context of obtaining the imaging quality of the full telescope optical system.

## 2 Phase measuring deflectometry

As this thesis makes use of the mirror measurement technique phase measuring deflectometry to derive a measure of the mirrors surface quality, its function principle will be explained in the following.

The phase measuring deflectometry (PMD) is a deflectometric method for the fast full-field measurement of specular free-form surfaces. It was developed by the Optical Sensing, Metrology and Inspection (OSMIN) group of prof. G. Häusler at the University of Erlangen-Nürnberg and is nowadays successfully applied in industry, e.g. for measuring eyeglass lenses (Häusler 1999). The basic idea of PMD is to evaluate the distortions of predefined patterns caused by reflection on the surface under test. The primary measure is the slope of the surface. In practice measurement uncertainties of around 150 arcsec (0.04 degree) can be achieved (Knauer 2006).

In the following chapter it is explained how the PMD method works and how it is applied to telescope mirrors. Measuring telescope mirrors implies relatively small curvatures, the existence of mathematical descriptions of the surfaces and according to that small shape deviations from those. For further details on PMD see Knauer (2006) and Häusler (1999).

### 2.1 From patterns to slopes

A typical PMD setup consists of a screen (e.g. a TV) that projects sinusoidal patterns, the reflecting surface under test and cameras taking pictures of the patterns reflected by the surface (see fig. 2.1). In order to measure large surfaces (e.g. telescope mirrors) it is also possible and sometimes even necessary to use multiple cameras to fully measure a surface. The single images are finally merged using the known cameras spatial positions and orientations.

Under the assumption of an ideal setup, the location, orientation and shape of the reflecting surface, the camera and the screen are known exactly. Accordingly the spatial coordinates of every single pixel of the screen respectively of the projected patterns and of the camera chip are known.

In this case the slopes can be determined as follows: If it would be known which pixel of the screen is depicted at which pixel of the camera, one could follow the sight rays of the camera pixels to the reflecting surface, connect the points of impact on the surface with the screen pixels mapped to the corresponding camera pixels and finally calculate the slope of the surface at the point of impact that is needed in order to legally connect camera and screen pixel. See figure 2.2 for illustration. The obtained slopes are the final result of the PMD evaluation.

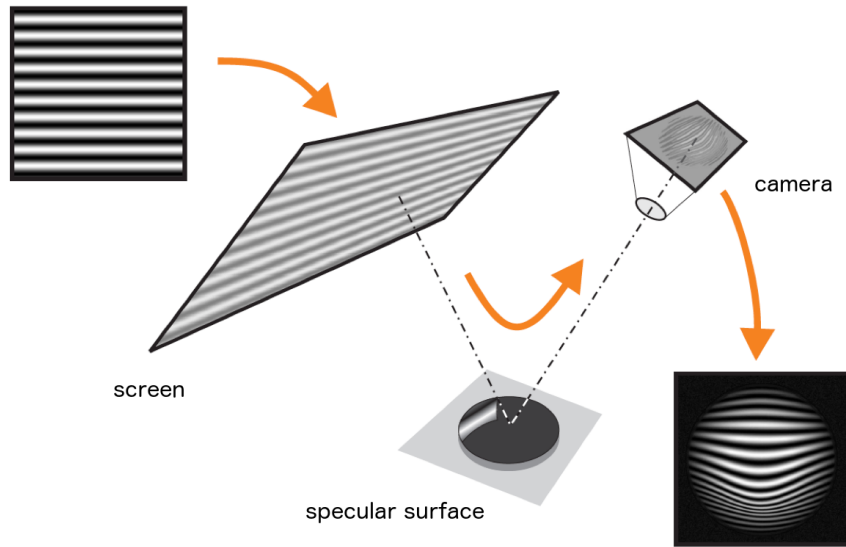


Figure 2.1: Sketch of a typical PMD setup. The sinusoidal pattern is projected on a screen. The camera observes the reflected and distorted pattern (Image from Knauer 2006).

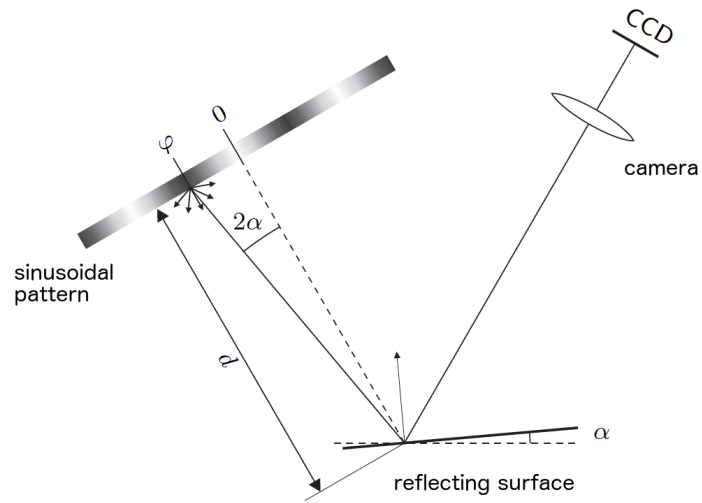


Figure 2.2: Observation of the sinusoidal pattern on the screen via the reflecting surface under test. The surface normal and slope can be calculated based on the screen to camera pixel mapping. The sine phase  $\varphi$  is a measure for the local slope  $\alpha$  (Image from Knauer 2006).



In a real measurement setup location, orientation and deformation of screen and cameras are calibrated and supposed to be known. Usually unknown is the location and orientation of the reflecting surface.

In the following, it will be explained how the screen to camera pixel mapping is achieved. Keep in mind that this is an essential step in the PMD measurement. Afterwards it will be explained how unknown locations, rotations and shape deviations of the reflecting surface under test are handled.

**Screen to camera pixel mapping** An essential step in the PMD method is to calculate which pixel of the camera maps which pixel of the screen as this information is needed for the determination of the slopes of the surface under test.

The simplest way to get this information is to switch on just one single pixel of the TV while all the others remain switched off and identify the camera pixel that maps the switched on screen pixel. As this has to be done for all pixels of the screen, the entire procedure would take a considerably long period of time, especially problematic regarding today's 4k TVs with more than 8 million pixels.

A much faster way to get the same information is to make use of sinusoidal patterns. Those are projected on the TV and observed by the camera. The obtained intensity distribution gives information about the sine phase in every pixel. Knowing the exact phase distribution of the sinusoidal pattern on the screen enables a determination of which pixel of the screen is mapped to which pixel of the camera. Applying the procedure for just one single pattern yields no clear screen pixel to camera pixel mapping due to the indistinguishable periodicity of the sine. At least a second sinusoidal pattern with a slightly different sine frequency that is coprime the first (typically 7 and 8 periods) has to be used. This allows a unique screen pixel to camera pixel mapping. In practice one captures also shifted versions of the same pattern in order to get better statistics for the determination of the phase. The standard method of shifting is the four shift: four sinusoidal patterns are shifted by a phase of  $\frac{\pi}{2}$  to each other and evaluated. As the low frequency patterns (typically 7 and 8 periods) have stripes that are too big for the application in PMD (see Knauer 2006) also patterns with a much higher frequency (typically  $24 \times 7$  and  $24 \times 8$  periods) which feature much thinner stripes are used. Due to a high noise level in the observed high frequency patterns those can not be used alone to calibrate the screen pixel to camera pixel mapping. Only the combined measurement of both — the low frequency and the high frequency patterns — allows an appropriate pixel mapping for the application in PMD.

A sinusoidal pattern encodes only one pixel dimension with a phase distribution. The screen pixel to camera pixel mapping can therefore just be solved in one dimension of the two dimensional screen. In order to completely map the full screen, sinusoidal patterns for both dimensions (horizontal and vertical) have to be used.

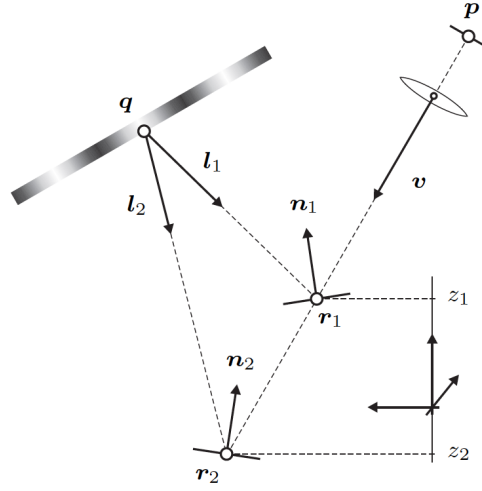


Figure 2.3: Ambiguity in PMD. Multiple surface height–slope combinations (here  $r_1, n_1$  and  $r_2, n_2$ ) lead to the same screen pixel  $q$  to camera pixel  $p$  mapping (Image from Knauer 2006).

**Variable location, orientation and shape deviations of the reflecting surface** During the measurement of a reflecting surface with unknown location, orientation and shape an ambiguity arises. With an unknown spatial surface distribution of the reflecting surface, multiple surface height–slope combinations are possible to construct a valid sight ray from the camera to the screen (see fig. 2.3). In Knauer (2006) this ambiguity is solved by an approach using a stereo camera setup.

In the case of measuring mirrors this approach is not possible as mirror surfaces do not provide fix points which are essential for the stereoscopic approach. For mirrors that are built according to a certain surface model (e.g. spherical or aspherical telescope mirrors) another approach has been found. The mirror can be evaluated with the help of its surface description. This allows to determine the best–fit location and orientation of the mirror in space: while keeping the camera sight rays fixed, the (reflecting) surface model is moved and rotated virtually until the discrepancy between the screen pixels which got hit by the reflected sight rays and the screen pixels that should be hit (determined by the screen pixel to camera pixel mapping) is minimal. It is assumed that the best–fit location and orientation of the mirror surface correspond to the real location and orientation of the measured mirror. Remaining discrepancies in the fit are due to surface irregularities of the mirror and are the measure of interest for following analysis. Based on the determined mirror position and orientation it is possible to derive the surface in space and to calculate the slopes like described above.

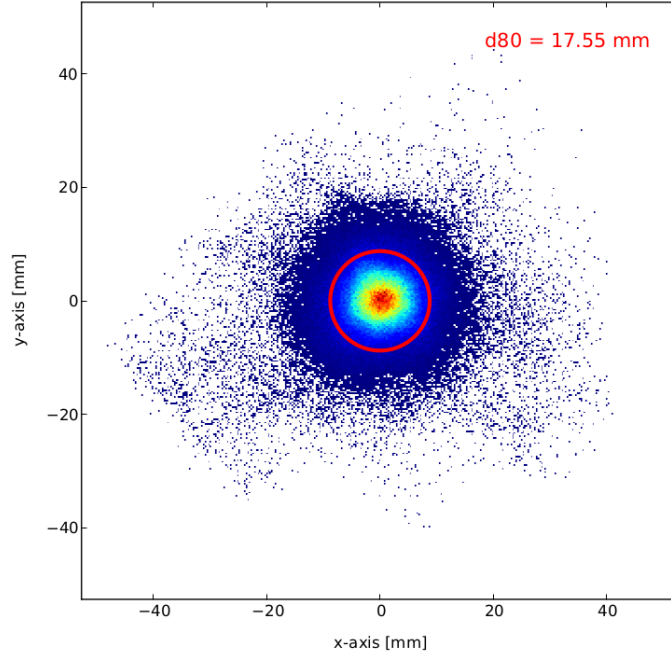


Figure 2.4: Example of a PSF of a spherical telescope mirror with a sphere radius of 32.3 m. The depicted d80 value defines the diameter of a circle with 80 % containment of the reflected light rays.

## 2.2 From slopes to the point spread function

Having calculated the slopes of the surface with PMD the point spread function (PSF) can be determined. The PSF is defined as the response of an imaging system to a point-like light source. It can be understood as the spatially resolved transfer function of the imaging system. For spherical mirrors the PSF is characterized by the d80 parameter which quantifies the point spread with the diameter of a 80 % containment circle.

In order to obtain the PSF, the slopes measured with PMD are virtually pinned to a surface which represents the mirror. Then light is emitted onto the mirrors surface. The light is represented by straight lines with an origin and a certain direction. Every light ray is reflected on the surface by using the determined slopes. The PSF is obtained by capturing the light in the focal plane of the mirror. It gives information about the imaging quality of the mirror and offers a possibility to analyze how light is distorted by the mirror.

Light captured beyond the focal plane results in a point spread (PS) that relates to the convolution of the original light source with the PSF. An example PSF is depicted in figure 2.4.

### 3 The Schwarzschild–Couder Telescope

Before turning to the PMD measurement of aspherical mirrors for the Schwarzschild–Couder Telescope (SCT), its design principle and the description of its mirrors are given in this chapter. Specific SCT designs for CTAs MSTs and SSTs exist. In the following it will be focused on the design chosen for the MSTs.

The SCT is a two–mirrored imaging atmospheric cherenkov telescope (IACT, Achary et al. 2013). The larger mirror, the so called primary mirror (P), reflects incoming light to a smaller one, the so called secondary mirror (S). Here the light is reflected onto the camera which is positioned between the primary and the secondary mirror. See figure 3.1 for illustration.

This setup is capable of covering a wide FOV providing an improved angular resolution compared to the traditional single–mirrored Davies–Cotton design. Additionally the SC optical design corrects for spherical and comatic aberrations (Byrum et al. 2015).

In the SCT design for the MSTs the mirrors P and S are both segmented in two affiliating rings P1 and P2 (S1 and S2 respectively) with numerous single mirror facets each.

At ECAP Erlangen a P1 mirror facet of the prototype SCT for the MSTs at CTA (code name P1.016) was available. Therefore the measurements later in this thesis as well as the following description of the telescope mirrors is focused on the P1 mirror facets.

In the following, the design of the SCT is described in detail. The mathematical description of its primary mirror is introduced and the mirror segmentation scheme is discussed. The curvature of the P1 mirror is investigated and its difference to a spherical surface is examined. The latter is interesting because the aspherical mirror facets will be evaluated under the assumption of a spherical surface model.

#### 3.1 Telescope design

The design of the SCT optical system (OS) is derived from the Schwarzschild aplanatic solution (Schwarzschild 1905) and is depicted in figure 3.2. The telescope features mirrors that have not a spherical shape. The focal plane (FP) of the SCT is bended.

The telescope design characterized by three parameters: the focal length  $F$ , the distance between the two mirrors  $\frac{F}{q}$  and the distance between the second mirror and the focal plane  $(1 - \alpha)F$  with auxiliary variables  $q$  and  $\alpha$ . It has been shown that values of  $q = \frac{2}{3}$  and  $\alpha = \frac{2}{3}$  optimize the performance of the SCT OS for the application in ground–based gamma–ray astronomy (Vassiliev et al. 2007; Vassiliev & Fegan 2007; Vassiliev & Rousselle 2012). The SC design following from these results provides a field of view of 8 degrees with a focal

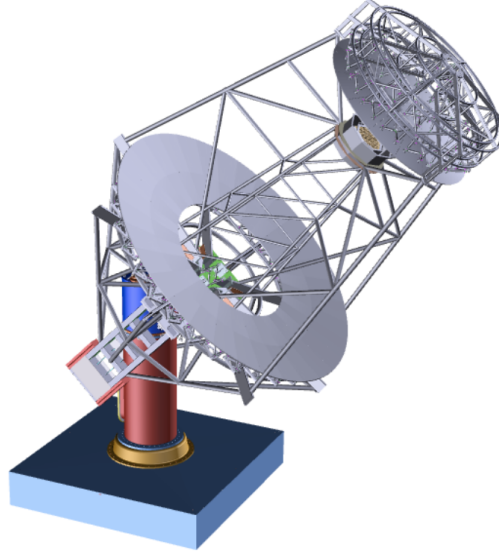


Figure 3.1: Schwarzschild–Coudé Telescope design. Primary mirror, secondary mirror and camera are visible (Image from Vandenbroucke 2014).

length of  $F = 5.59$  m and an effective light collecting area of  $50 \text{ m}^2$ . The mirror dishes have a diameter of 9.66 m and 5.42 m respectively and a distance of 8.38 m.

### 3.2 Mirror segmentation

In the SCT design for the MSTs the two mirrors are each segmented in two rings with 16 and 32 elements for the primary mirror P and 8 and 16 elements for the secondary mirror S. One mirror element of the inner ring touches two elements of the outer ring (see figure 3.3, Rousselle & Vassiliev 2013). All elements that are of the same type (belong to the same ring of the same mirror) are identical due to rotational symmetry. Table 3.1 summarizes the important parameters of the mirror segmentation.

From now on, mirror facets of the inner ring of the primary mirror (P) will be referred as P1–mirrors. In analogy to that P2 mirrors belong to its outer ring.

### 3.3 Mathematical mirror description

The Schwarzschild aplanatic solution gives the exact analytical surface description for both of the mirrors. There is also an approximating polynomial for each. The surface definition is rotationally symmetric and the height of the mirror surface as well as its slope depend only

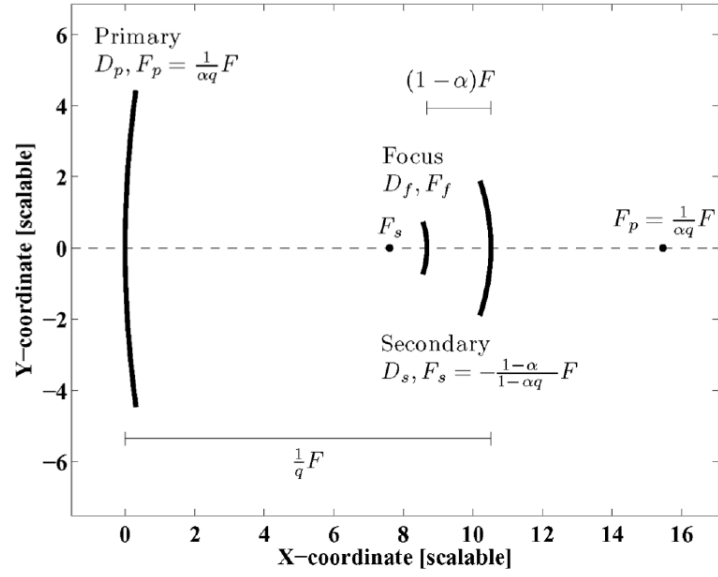


Figure 3.2: Geometrical design of the SCT optical system (figure from Vassiliev & Rousselle 2012). It is defined by the parameters  $F$  (focal length),  $q$  and  $\alpha$  that define the relative positioning of the primary and secondary mirrors and the focal plane of the whole system.

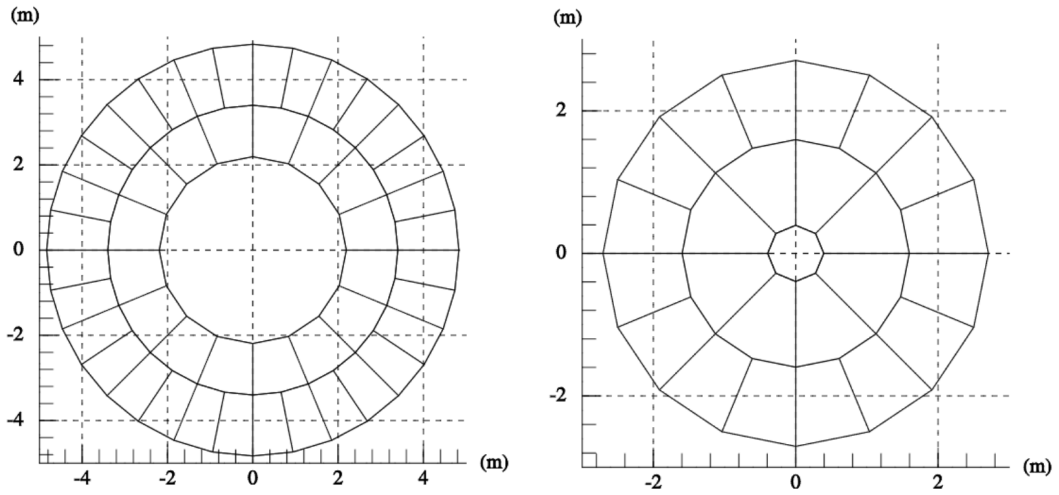


Figure 3.3: Segmentation scheme for primary (left) and secondary (right) mirror (Image from Rousselle & Vassiliev 2013).

	Primary mirror		Secondary mirror	
	inner (P1)	outer (P2)	inner (S1)	outer (S2)
Number of segments	16	32	8	16
Angular coverage [deg]	22.5	11.25	45	22.5
Radial coverage [m]	2.19350	3.4000	0.3945	1.5965
	-	-	-	-
	3.4000	4.831875	1.5965	2.7083

Table 3.1: Parameters of the mirror segmentation (Rousselle &amp; Vassiliev 2013).

on the radius<sup>1</sup>. Both definitions are given in cylindrical coordinates. As this thesis only deals with a P1 mirror element, only definitions referring to the primary mirror are given in the following. The next paragraph follows Vassiliev & Rousselle (2012) which contains more detailed explanation and also the definition of the secondary mirror.

**Surface definition** An infinitesimal surface element of the primary mirror can be approximated by a cylinder. With  $\tau = \left(\frac{r^2}{F^2}\right)$  where  $r$  is the radial distance to the optical axis of the telescope, the mirror surface is given by:

$$\frac{x(\tau, \phi)}{F} = \sqrt{\tau} \cos \phi \quad (3.1)$$

$$\frac{y(\tau, \phi)}{F} = \sqrt{\tau} \sin \phi \quad (3.2)$$

$$\frac{z(\tau)}{F} = Z(\tau) \quad (3.3)$$

$\phi$  is the angular coordinate and  $x$ ,  $y$  and  $z$  are the three spatial coordinates in a Cartesian coordinate system. In its exact analytical definition  $Z(\tau)$  has the form:

$$Z(\tau) = \frac{1}{486} \frac{\tau}{(1 + \sqrt{1 - \tau})^3} (47 + 141 \sqrt{1 - \tau} + 171(1 - \tau) + 73(1 - \tau)^{1.5}) \quad (3.4)$$

In its approximative definition, which can be obtained by a Taylor expansion around  $t = \tau - \frac{7}{16}$ ,  $Z(\tau)$  has the form:<sup>2</sup>

$$\begin{aligned} Z(t = \tau - \frac{7}{16}) = & 3.7728 \times 10^{-5} + 0.11103t - 6.1287 \times 10^{-3}t^2 - 7.4068 \times 10^{-3}t^3 \\ & + 1.6205 \times 10^{-2}t^4 - 4.5056 \times 10^{-2}t^5 + 7.4550 \times 10^{-2}t^6 \\ & - 8.3673 \times 10^{-2}t^7 + 5.5009 \times 10^{-2}t^8 - 1.7286 \times 10^{-2}t^9 \end{aligned} \quad (3.5)$$

<sup>1</sup>The mirrors surface height also depends on the focal length  $F$  but  $F$  is treated as a constant.

<sup>2</sup>According to Vassiliev & Rousselle (2012), using a polynomial of degree of at least 6 is recommended but degree 9 is preferable. According to that they give the expansion coefficients for polynomials of degree 7 to 11.

**Surface normals** Given the analytical definition of the mirrors the exact surface normal at any point on the surface can be determined by calculating the cross product between radial and angular derivatives of  $\vec{r}(r, \phi) = (x(r, \phi), y(r, \phi), z(r))^\mathbf{T}$  with  $r = F \sqrt{\tau}$ :

$$\vec{n}|_{r,\phi} = \left( \frac{d\vec{r}(r, \phi)}{dr} \times \frac{d\vec{r}(r, \phi)}{d\phi} \right)_{r,\phi} \quad (3.6)$$

$$= r \cdot \begin{pmatrix} -\frac{2r}{F} \cdot \frac{dZ(\tau)}{d\tau} \cdot \cos \phi \\ -\frac{2r}{F} \cdot \frac{dZ(\tau)}{d\tau} \cdot \sin \phi \\ 1 \end{pmatrix} \quad (3.7)$$

with given  $Z(\tau)$  (see last paragraph) and its derivative which can be calculated as:

$$Z(\tau) = \frac{1}{486} \cdot A \cdot B \quad (3.8)$$

$$\frac{dZ(\tau)}{d\tau} = \frac{1}{486} \cdot \left[ \frac{dA}{d\tau} B + A \frac{dB}{d\tau} \right] \quad (3.9)$$

$$A = \frac{\tau}{(1 + \sqrt{1 - \tau})^3} \quad (3.10)$$

$$B = (47 + 141 \sqrt{1 - \tau} + 171(1 - \tau) + 73(1 - \tau)^{1.5}) \quad (3.11)$$

$$\frac{dA}{d\tau} = \frac{\tau + 2(1 + \sqrt{1 - \tau})}{2 \sqrt{1 - \tau} (1 + \sqrt{1 - \tau})^4} \quad (3.12)$$

$$\frac{dB}{d\tau} = -70.5 \sqrt{1 - \tau}^{-1} - 171 - 109.5 \sqrt{1 - \tau} \quad (3.13)$$

### 3.4 Curvature and focal planes

Parallel light traveling along the optical axis (o. a.) of a mirror is reflected to the mirrors focal point. This point is located in a distance to the mirror which is called focal length ( $f$ ). The plane at the focal point orthogonal to the o. a. is called the focal plane (FP).

The curvature radius is linked to the focal length by a factor of 2. This can be understood by the help of geometrical considerations. The surface normal in each point of a sphere always points to the spheres center. As for reflections the incident angle to the surface normal equals the emergent angle, light aligned parallel to the optical axis of a spherical mirror is reflected to half of the curvature radius of the representing sphere to the focal point in focal length  $f$ . Accordingly the focal length is half the curvature radius.

Aspherical mirrors have an astigmatic form and therefore feature two different curvatures. One corresponds to the radial base vector  $\hat{r}$  which will be called **tangential curvature** and



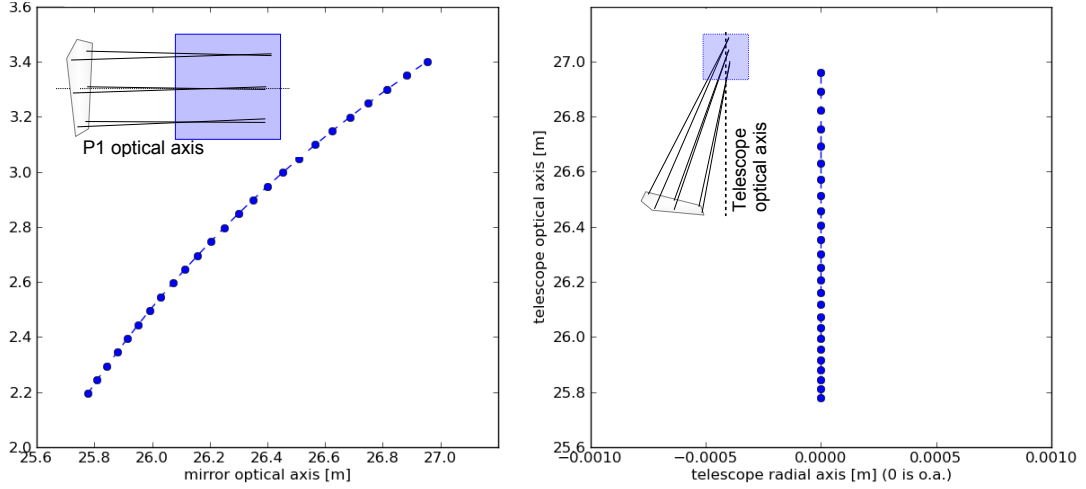


Figure 3.4: Distribution of the sagittal curvature radius relatively to the o. a. of the mirror facet (left) and to the o. a. of the SCT (right).

the other one corresponds to the angular base vector  $\hat{\phi}$  which will be called **sagittal curvature**. The curvatures of the P1 mirror type are different enough that both can be distinguished.

The sagittal curvature is distributed homogeneously along the angular axis  $\phi$  and decreases with radial distance  $r$  which results in a certain curvature radius for a certain radial distance. Therefore the sagittal curvature is the highest at the lower end of the mirror facet (smallest  $r$ ) and the lowest at the upper end (largest  $r$ ). Investigating several radial distances for the corresponding sagittal curvature radius yields the sagittal curvature radius distribution which corresponds to a bent shape of the FP. The distribution of the sagittal curvature radius is depicted in figure 3.4 (left). Placing the mirror in the telescope clarifies the existence of the specific distribution of curvature radii. Figure 3.4 (right) shows, that the distribution of the sagittal curvature is concentrated on the o. a. of the telescope.

The tangential curvature is inhomogeneously distributed along the radial axis  $r$  and does not vary along the angular axis  $\phi$ . This inhomogeneity yields no clear curvature radius.

Figure 3.5 illustrates the position of sagittal and tangential curvature radii. The range of the distribution of the sagittal curvature radii is sketched as the box.

So, both curvatures can not be described by a single radius and accordingly have no clear focal point. Measurements of PSs of mirrors are usually performed with plane sensors. With plane sensors it is not possible to measure the full FP at a time. Instead the measured PS contains a focused part and a much larger part which is out of focus.

A single line would be obtained as a PS if it would be possible to exactly follow the distribution of curvature radii. Accordingly the d80 parameter used for spherical mirrors is

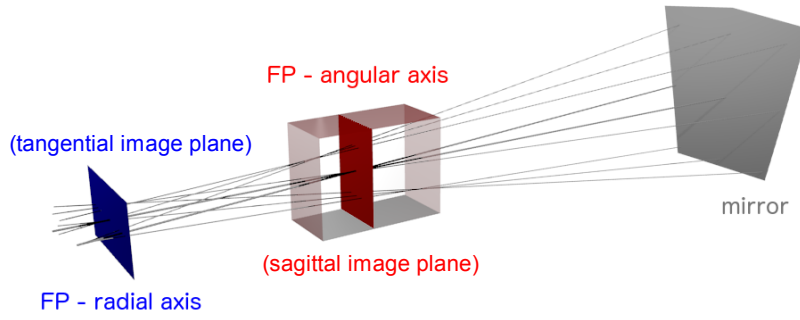


Figure 3.5: Illustration of the curvature radii of the aspherical P1 mirror. The planes represent the averaged sagittal and tangential curvature radius respectively. The wide range of the distribution of the sagittal curvature radii is sketched as the box.

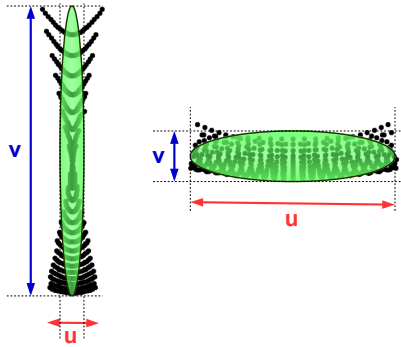


Figure 3.6: Point spreads with minimal diameters  $u$  and  $v$  respectively. Sketches of the describing ellipses are printed over the PSs. It can be seen, that both PSs contain focused areas and areas that are out of focus.

not applicable because it describes a circular containment. Instead, the PS is described as an ellipse with two individual diameters  $u$  and  $v$ . This allows to characterize the point spread for sagittal and tangential curvature independently. The diameters  $u$  and  $v$  are determined as the standard deviation of the point spread in the corresponding axis. The PSF for both curvatures is related to the PSs with minimal  $u$  and  $v$  respectively. The distance to the mirror in which the minimal  $u$  and  $v$  can be observed corresponds to the most suitable curvature radius. Figure 3.6 shows the PSs with minimal  $u$  and  $v$  respectively obtained from the P1 mirror using a plane sensor. The describing ellipses are sketched.

### 3.5 Comparison of aspheres and spheres

As the standard PMD evaluation makes use of a spherical surface model, the difference between spherical and aspherical surface models are investigated. The model of the P1 mirror facet will be compared to a best fit sphere. Figure 3.7 shows the spatially resolved surface height difference between the aspherical and the best fit spherical surface. Height differences of up to  $\pm 320\text{ }\mu\text{m}$  are visible. The fit has positioned the sphere around the center of the mirror with a radius that lies in between of the tangential and the sagittal curvature radius. The bluish areas along the radial axis of the mirror illustrate that the tangential curvature radius is larger than the radius of the fitted sphere. The reddish areas along the angular axis of the mirror illustrates that the sagittal curvature radius is smaller than the radius of the fitted sphere. In the next chapters it will be shown how this height differences affect the evaluation procedure of the aspherical P1 mirror.

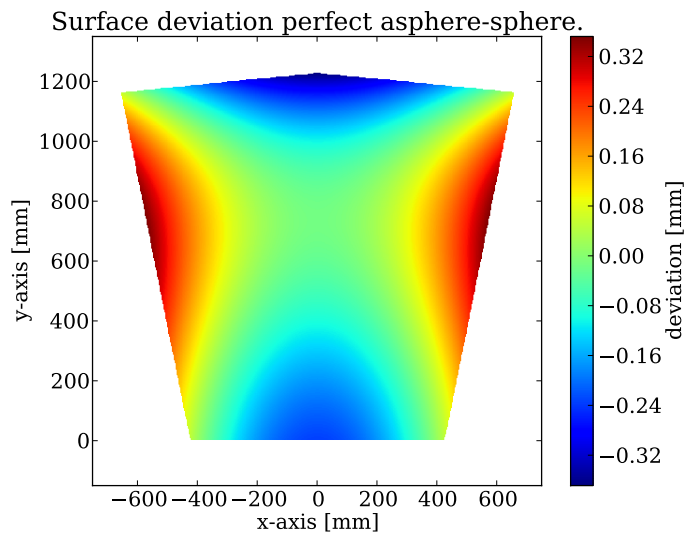


Figure 3.7: Height difference between the aspherical P1 mirror model and an aligned sphere. Height differences of up to  $\pm 320\mu\text{m}$  are visible. The radius of the sphere was fitted in between the curvature radii of the aspherical mirror model.

## 4 Simulating aspherical mirror facets

Before real aspherical mirrors are measured with PMD using the standard PMD evaluation, it is investigated which results can be obtained for ideal aspherical mirrors. This is achieved with the help of simulated datasets. How aspherical mirrors are integrated in simulations of PMD measurements is shown in the following.

Simulations of PMD measurements of spherical telescope mirrors have been developed by Pickel (2014). In this thesis the setup of a PMD measurement setting was emulated in a ray tracer in order to simulate the images real cameras would take during a PMD measurement. The resulting images were evaluated with the standard PMD evaluation for real measurements. In the simulation a segment of a perfect sphere was used to model the measured spherical mirror facets. Spheres are standard shapes with a rather simple analytical description and therefore are a built-in feature of the ray tracer. Due to their complex surface, there is no closed solution for simulating aspherical mirrors in the same way. In order to study systematics of the evaluation procedure, it is necessary to develop an appropriate approach to simulate PMD measurements with aspherical mirror facets.

For this purpose the surface of the aspherical P1 mirror has been approximated by a finite amount of triangles covering the reflecting mirror surface. By using this technique it is possible to directly integrate a P1 mirror facet in the ray tracing set up by Pickel (2014).

In this chapter an introduction to simulating PMD measurements is given. It is explained how aspherical P1 mirrors are integrated in these simulations. The results of the applied PMD evaluation on simulated PMD measurements are shown in chapter 5.

### 4.1 Introduction to simulating PMD measurements

As explained in Pickel (2014), the ray tracer *Mitsuba*, a physically based renderer (Wenzel 2014), is used to emulate a PMD measurement of spherical mirrors.

Ray tracing is a computer based technique for generating images by tracing the path of light rays and simulating their interactions with virtual objects in the simulated scene (Wenzel 2014).

Emulating a PMD measurement works as follows: typically four cameras, a screen projecting the sinusoidal patterns and the mirror under test are placed virtually in a scene. For the measurement of spherical mirrors, the mirror is modeled as a reflecting segment of a perfect sphere. The screen emits light rays carrying the black and white color information of the projected sinusoidal pattern. These light rays are traced in the scene. Some of them are reflected by the mirror segment and hit the virtual cameras. Here they form images of the

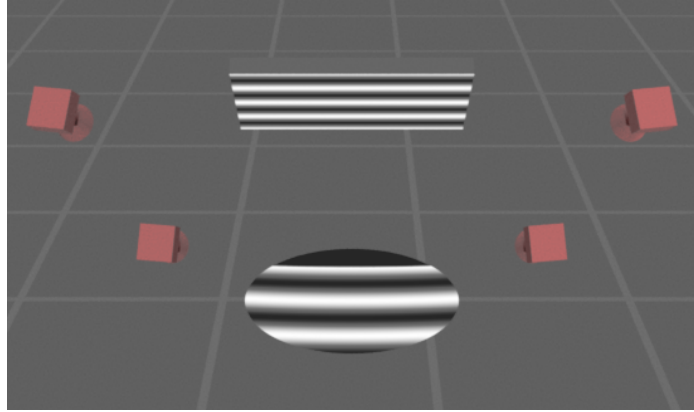


Figure 4.1: Example setup of a simulated PMD measurement. The screen with projected sinusoidal pattern, a spherical mirror facet at the bottom and four cameras are depicted.

reflected and distorted sinusoidal patterns just like in a real PMD measurement. Figure 4.1 illustrates an example setup of a simulated PMD measurement and figure 4.2 shows images taken during a simulated and a real PMD measurement.

## 4.2 Integration of aspherical mirrors in PMD simulations

As mentioned above a new approach has to be developed for simulating aspherical mirrors. For this purpose the surface of the aspherical mirror P1 has been approximated by a finite amount of triangles covering the reflecting mirror surface. These sets of triangles are usually called *meshes* (Bender & Brill 2006).

**Meshes and shading** Meshes are a common way in computer graphics to easily describe even highly complex surfaces and are therefore also supported in the most available ray tracing frameworks. A mesh consists of the spatial positions of several nodes called *vertices*, information that connects specific vertices to *faces* (e.g. triangles) and optionally a vertex normal for each vertex.

The latter is necessary for the shading. Shading denotes the mechanism how reflection of light on a surface is handled. One distinguishes between flat and smooth shading. These methods differ in the way of computing the normal for reflection:

For *flat shading* the exact surface normal at the intersection point of the light ray with a face of the mesh is not relevant for reflection. Instead, the face normal of the intersected face is used as the normal at the intersection point. The face normal can be computed as the cross product of two edges connecting each two vertices of the face. In this case there is only a finite amount of discrete normals corresponding to the degree of discretization.

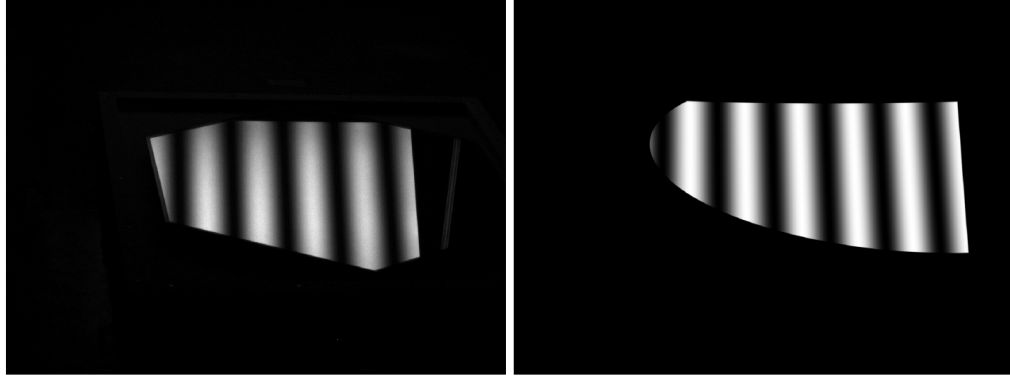


Figure 4.2: Image taken from a camera in a real PMD setup (left) and a simulated one (right). The reflecting surfaces were spherical mirrors in both cases (Images from Pickel 2014).

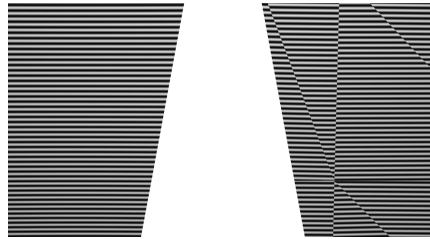


Figure 4.3: Shown are two excerpts of the same aspherical mirror mesh with a wide grid cell size reflecting a sinusoidal pattern. Note the difference in smooth shading (left) and flat shading (right). For the flat shaded mirror the single faces of the mesh are clearly discernible. The difference between both shading modes is noticeable although the camera in this scene was placed far out of the focal plane of the mirror.

Therefore, the quality of the resulting image strongly depends on the degree of discretization of a smooth surface.

In *smooth shading* the normal at intersection point is calculated as the linear weighted average of the vertex normals belonging to the corners of the face that was hit. The advantage compared to flat shading is a continuous behavior of the normals that leads to smooth looking surfaces in a ray tracing. Even if the underlying surface does not perfectly fit the linear weighting in the normal averaging one can find a degree of discretization where the resulting error will be negligible (Gouraud 1971; Phong 1975). The disadvantage is that one normal for each vertex of the mesh has to be defined in advance.

Figure 4.3 illustrates the difference between both shading modes. In summary: highly accurate smooth shading has to be possible for the mesh of the mirror. Therefore vertex normals have to be created.

In the following it is explained how meshes for aspherical mirrors can be formed. It is discussed how vertices are spread over the surface and how the corresponding vertex normals for smooth shading are found.

**Building the mirror mesh** As the mathematical mirror description of the P1 mirror is given in cylinder coordinates, the easiest method of distributing points over the mirror surface is by using a polar method. The surface height can be calculated by using the radius. The parameters that define a discretization in this case are a radial  $r_{\text{discrete}}$  and an angular  $\phi_{\text{discrete}}$  degree of discretization. Applying the polar method has the disadvantage of a non constant point density on the mesh due to divergent radial lines. In the sense of smooth shading a decreasing point density causes an increasing systematic error during normal interpolation and therefore for light reflection angles.

To avoid this points are distributed over the mirror surface using a Cartesian grid. This complicates edge treatments but ensures a constant point density on the inside of the mesh. Furthermore projection of the regular grid on the bent surface has still to be taken into account. Otherwise the point density would vary inversely with the slope of the surface.

Having all vertices distributed over the mirror surface they are connected to triangles to form a closed surface. The vertex normals for each vertex equal the exact surface normal at the certain vertex and can be computed using formula 3.6 from chapter 3.3.

All meshes produced are built using a Cartesian grid spacing. A sketch of a mesh created for the P1 mirror facet can be seen in figure 4.4.

**Finding the optimal degree of discretization** Even if the underlying surface is not homogeneous enough to perfectly fit the linear weighting during the vertex normal averaging in smooth shading, it is possible to find a fine degree of discretization where the resulting error for the averaging is negligible.

In order to find a sufficient degree of mesh discretization a ray tracing with parallel incoming light aligned to the optical axis of the P1 mirror facet was performed and the re-



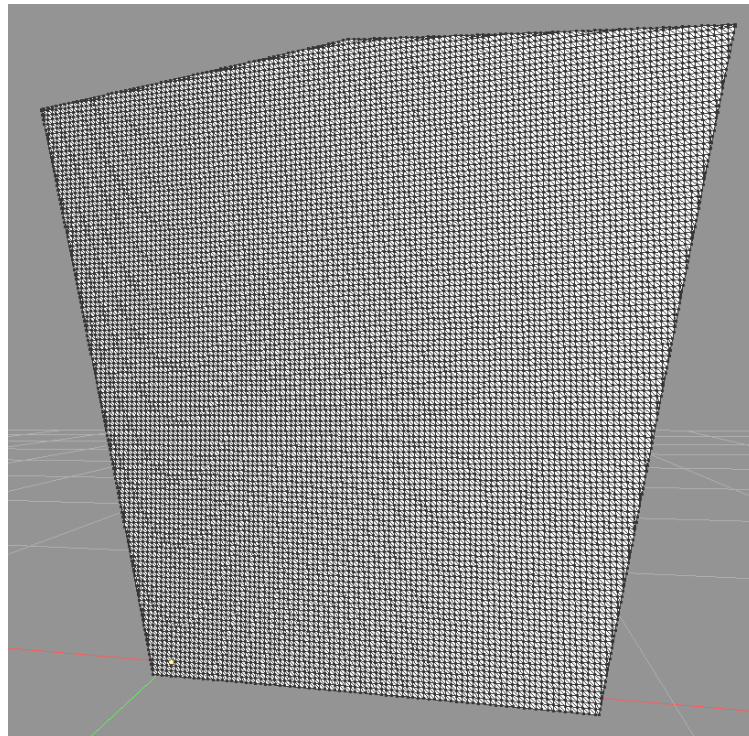


Figure 4.4: Sketch of a mesh created for the P1 mirror. Shown are the vertices and edges that form the triangles. The mesh has been created with a mesh cell size of  $1 \times 1 \text{ cm}^2$ .

curvature type	focal length to mirror	curvature radius
sagittal	13.18 m	26.36 m
tangential	14.59 m	29.18 m

Table 4.1: Obtained focal lengths and the corresponding curvature radii for sagittal and tangential mirror curvature for the P1 mirror mesh with a grid cell size of  $10 \times 10 \text{ mm}^2$ .

sulting focal planes were analyzed. For different mesh cell sizes ranging from  $2 \times 2 \text{ mm}^2$  to  $90 \times 90 \text{ mm}^2$  the focal lengths and the broadening of the PS described by the parameters  $u$  and  $v$  were determined. Both parameters should stabilize if the mesh is fine enough that a further decrease of the edge length of the cells would not enhance the reflection quality anymore. The focal lengths of sagittal and tangential curvature and the spread values of  $u$  and  $v$  at the focal plane obtained by the ray tracing are shown in figure 4.5. The sagittal focal length and its spread converge for mesh discretizations finer than a grid cell size of  $20 \times 20 \text{ mm}^2$  whereas for resolving the tangential curvature grid cell sizes of smaller than  $40 \times 40 \text{ mm}^2$  seem to be sufficient. It was decided to use a mesh discretization with grid cells of dimension  $10 \times 10 \text{ mm}^2$ .

Using the chosen discretization, a PS scan during a ray tracing yields the point spread parameters  $u$  and  $v$  as a function of distance to the mirror shown in figure 4.6. The minima in these distributions define the characterizing sagittal and tangential focal lengths and the corresponding curvature radii of the ideal P1 mirror. The obtained focal lengths and curvature radii are shown in table 4.1.

An example scene of a simulated PMD measurement using the above generated aspherical P1 mirror mesh can be seen in figure 4.7.

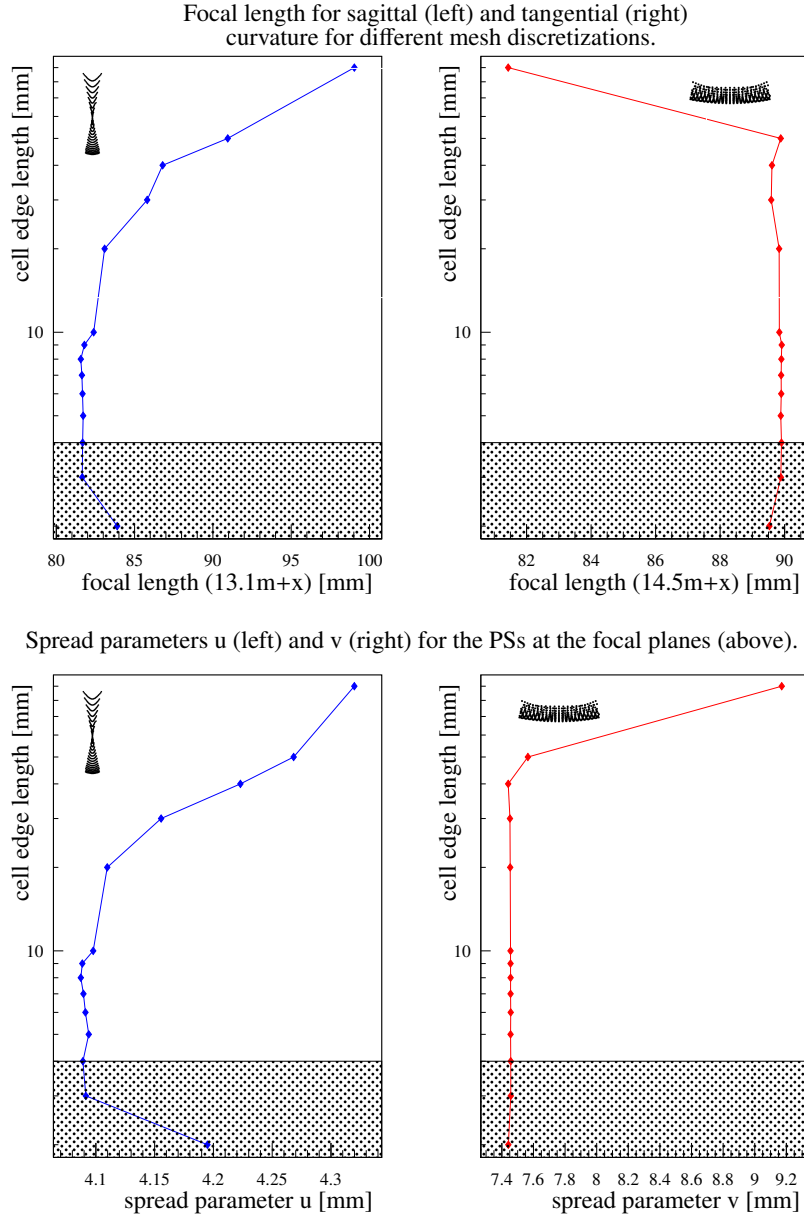


Figure 4.5: Determined focal lengths for sagittal and tangential curvature (top) and the corresponding  $u$  and  $v$  point spread diameters (bottom) for different mesh discretizations as a function of mesh discretization. The values stabilize for grid cell sizes of smaller than  $20 \times 20 \text{ mm}^2$ . For grid cell sizes smaller than  $4 \times 4 \text{ mm}^2$  the edge treatment in the mesh creation algorithm is not reliable. The data taken in this regime is marked out.

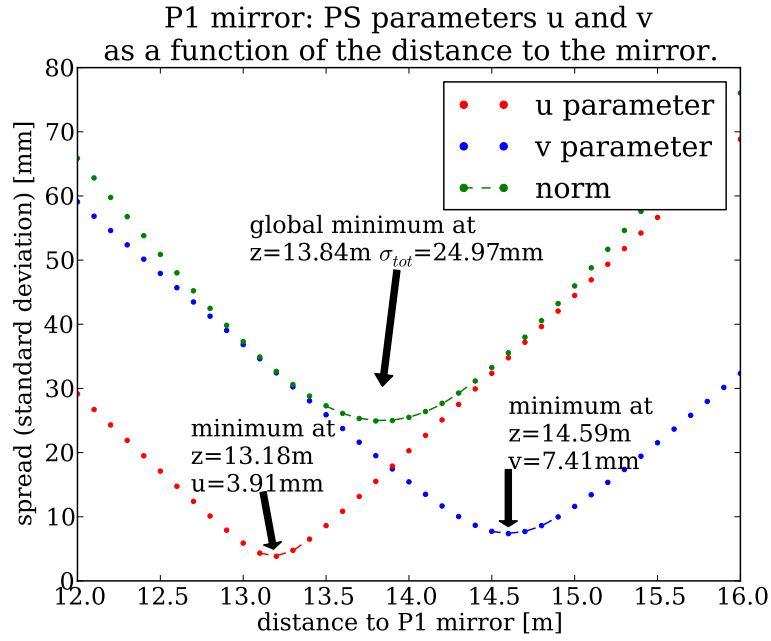


Figure 4.6: Distribution of the PS parameters  $u$  and  $v$  as a function of distance to the mirror along the o. a. The focal length of the sagittal curvature (red) and tangential curvature (blue) can be obtained from the minima. Also the total PS spread is depicted (green). A discretization of  $10 \times 10 \text{ mm}^2$  is used for the mirror mesh.

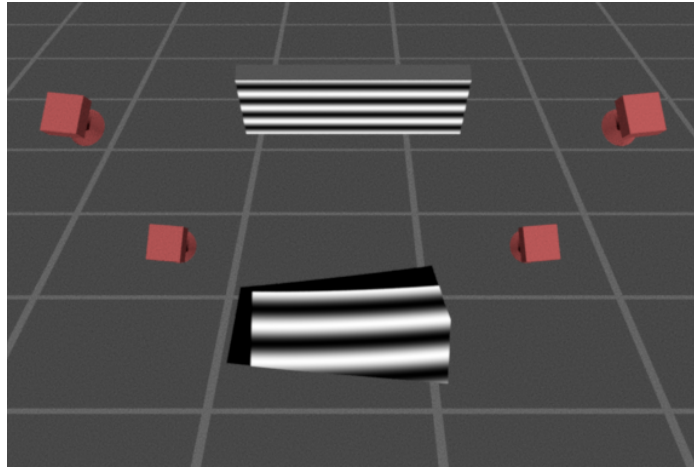


Figure 4.7: Example setup of a simulated PMD measurement with an aspherical P1 mirror is shown. The screen with projected sinusoidal pattern, the aspherical P1 mirror mesh and four cameras are depicted.

## 5 Measuring ideal aspherical mirror facets with a spherical surface model

In the last chapter it has been shown how PMD measurements of ideal aspherical mirrors can be simulated. The PMD evaluation will be applied to these simulated measurements in the following. It is shown which modifications to the existing evaluation procedure for spherical mirrors are applied and which results can be achieved.

As explained in chapter 2 the applied PMD evaluation procedure makes use of an underlying surface model for the measurement object to get rid of the ambiguity in PMD. Figure 5.1 illustrates the evaluation result of an example simulation of a PMD measurement of a spherical telescope mirror using four cameras showing the determined slopes in one direction and the final PSF obtained with a ray tracing. It has been shown that the developed procedure works quite well for the measurement of spherical telescope mirrors (see e.g. Wörnlein 2012).

Due to the complex shape of aspherical mirrors, it is not handy to implement the same technique based on the exact aspherical surface model. This chapter follows the approach of applying the standard PMD evaluation procedure for spherical mirrors, which assumes a spherical surface model for the measurement object, to the ideal aspherical P1 mirror. The problems and limits connected to this approach are pointed out. Additionally, three ways of investigating the measured aspherical mirrors quality will be investigated.

### 5.1 Image merging quality

For measuring telescope mirrors multiple cameras are needed in order to be able to fully measure the mirror surface like it is described in chapter 2. Typically environmental influences lead to a slight displacement and rotation of all components in the measurement setup relatively to their nominal, calibrated state. As the knowledge of the exact position and orientation of all the cameras in the setup is essential for merging the single images from every camera to one single result, a recalibration of all cameras is applied in every evaluation process in order to enhance the measurement quality.

During these recalibrations a first rough virtual positioning of the underlying mirror surface model is performed as it is described in chapter 2.1. During this first step of recalibration the camera positions and orientations are fixed to their last calibrated state. In a next step the positions and orientations of all cameras are freed and it is tried to enhance the measurement quality by adjusting these.

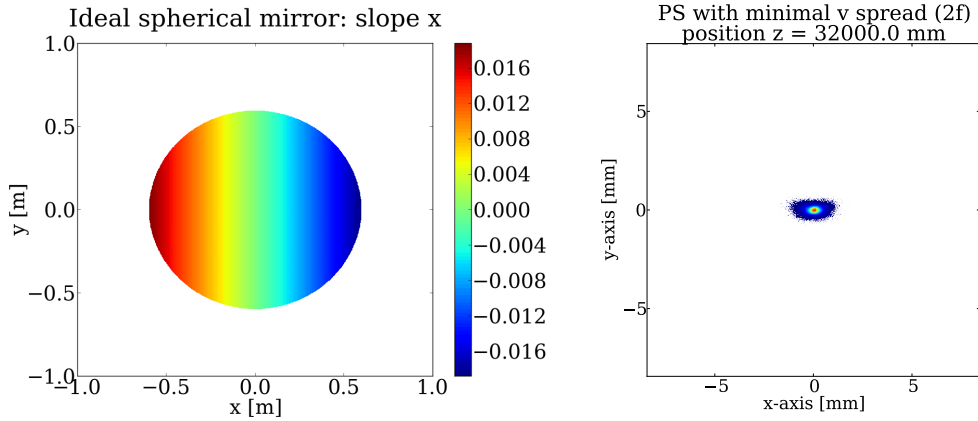


Figure 5.1: PMD evaluation result of a simulated spherical mirror with curvature radius 32 m. Slopes in x-direction (left) and ray traced PSF (right) are shown. The FP can clearly be resolved during ray tracing.

In the presence of more than one camera in the setup, assuming a spherical surface model for measuring an aspherical shape induces problems. Every camera observes a different surface element of the asphere. So each of the cameras is repositioned during the calibration process in the way that its measured aspherical surface element is aligned best to the used spherical surface model which leads to wrong camera positions and orientations. As a result, the individual images can not be merged adequately and deviating slopes are determined for the cameras. Figure 5.2 shows the result from the evaluation of a simulated four camera PMD measurement of an aspherical telescope mirror applying the described evaluation procedure. Visible is the inadequate merging of the four camera images due to falsely recalibrated camera parameters. This results in FPs that are not evaluable (see figure 5.2, right).

This problem can be solved by measuring the aspherical mirror in combination with a spherical reference mirror. The reference mirror is used for recalibrating the setup while the aspherical mirror is actually measured. Figure 5.3 shows the result from the evaluation of the same simulated four camera PMD measurement of the aspherical telescope mirror as above with the difference that the spherical mirror shown in figure 5.1 was used as the reference mirror for camera calibration. The merged image now has the same quality like for the associated one for the simulated spherical mirror alone (see figure 5.1). By using the shown evaluation technique a distinction of both focal planes during the ray tracing is possible (see figure 5.3, right).

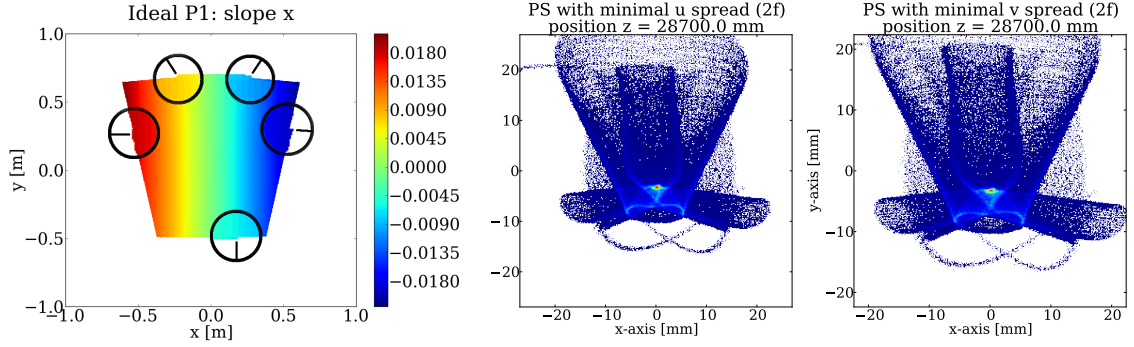


Figure 5.2: PMD evaluation result of a simulated aspherical mirror. Slopes in  $x$ -direction (left) and ray traced PSF (right) are shown. Note the edges in the resulting image emphasized by the markers (left, slope  $x$ ). The image is zoomed inside the markers. The individual FPs can not be resolved during ray tracing as shown in the point spreads with minimal  $u$  and  $v$  parameters (right). See appendix A for larger image.

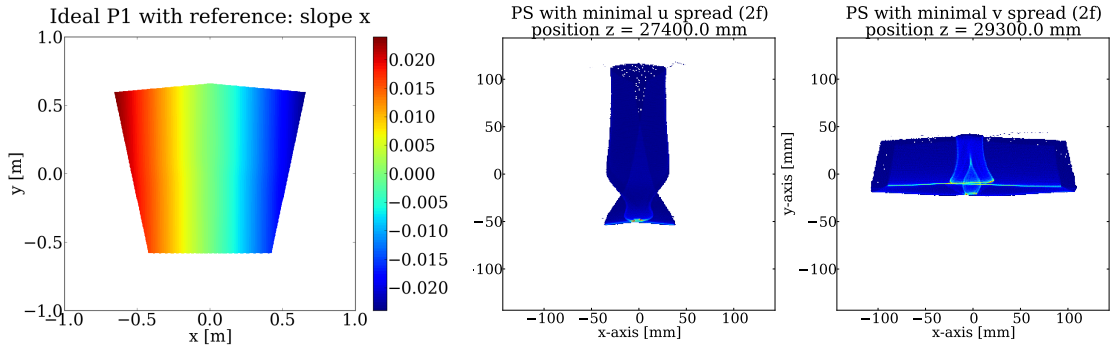


Figure 5.3: Evaluation result of a simulated aspherical P1 mirror using a spherical reference mirror for camera recalibration. Slopes in  $x$ -direction (left) and corresponding ray traced PSF (right) are shown. Note the improved image merging quality (left, slope  $x$ ). The individual FPs are distinguishable during ray tracing (right).

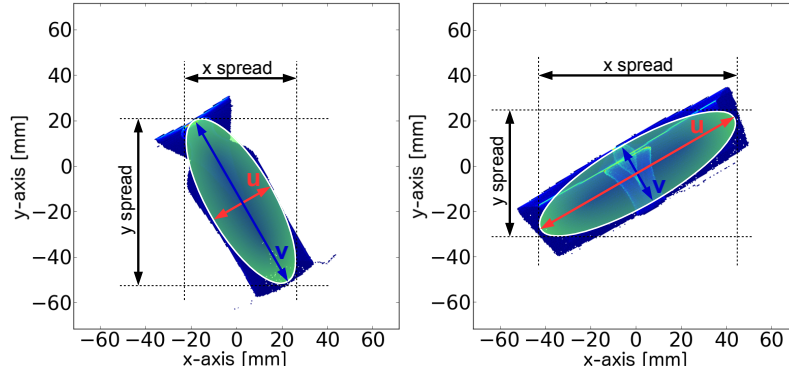


Figure 5.4: Shown are example PSs for the sagittal and tangential curvature of a ray traced ideal P1 mirror. The mirror was rotated with -150 degree. Not the spread in x- and y-direction is relevant but indeed the diameters  $u$  and  $v$  defining the describing ellipse.

## 5.2 Determination of curvature radii and the importance of mirror orientation

In the following, the curvature radii of measured mirrors are determined with a ray tracing. Light rays propagate onto the mirrors surface model which is a perfect sphere in the standard PMD evaluation. The light rays are reflected on the surface by using the slopes obtained with PMD. The focal length of the measured mirror can be obtained by using light rays that propagate parallel to the optical axis of the measured mirror. This method is called 1f measurement. The curvature radius can be obtained by sending out light to the mirror surface originating from a point source located on the optical axis. The reflected light is then analyzed at the point of emission. This method is called 2f measurement. To obtain the focal length and the curvature radius the PSs of the reflected light are scanned for minimal  $u$  and  $v$  values along the optical axis of the mirror. Measuring both quantities works as a cross check as the focal length and the curvature radius have to be connected by a factor of 2.

Note, that  $u$  and  $v$  are defined as the diameter of the ellipse describing the PS and represent the standard deviation of the PS along the main axes of the ellipse. For mirror facets that are aligned to the internal coordinate system of the PMD measurement setup the  $u$  and  $v$  parameters correspond to the setups Cartesian coordinate axes. For tilted mirror facets also the observed PS tilts and the describing ellipse is adjusted in order to fit the PS. Therefore the parameters  $u$  and  $v$  describe the PS independently of a mirror tilt. Figure 5.4 shows a ray traced PS from a tilted mirror and the appropriately describing ellipse.

In the following, the ideal P1 mirror will be measured in two orientations: the common mirror placement and the corresponding orthogonal mirror placement. Figure 5.5 illustrates the difference between both orientations.



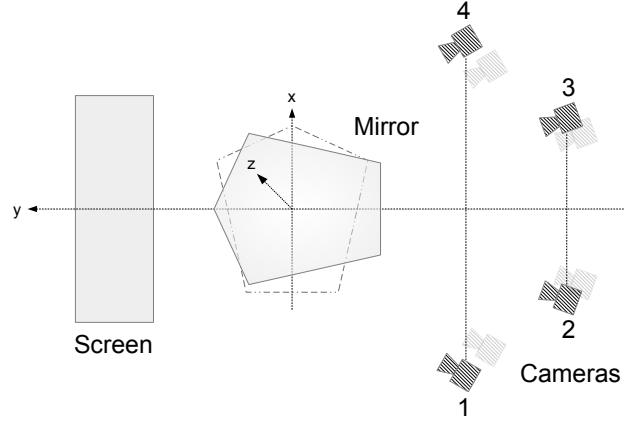


Figure 5.5: Sketch of the simulated PMD measurement setup. The measured aspherical mirror is depicted in the common orientation with its tip pointing to the screen and in the corresponding orthogonal one.

**Common mirror placement** An ideal P1 mirror has been simulated, measured and evaluated. The mirror was placed in the measurement setup with its tip pointing to the screen, the so called common placement (see figure 5.5). It will be shown in the following that it makes a difference in which orientation the mirror is measured. Figure 5.6 shows the dependency of the obtained parameters  $u$  and  $v$  on the distance to the mirror along its o. a. Its subfigures show the results obtained from the simulated spherical mirror (a), the simulated aspherical mirror evaluated without a reference measurement (b) and the simulated aspherical mirror evaluated with the spherical reference mirror (c). The corresponding point spread functions at the FPs can be found in figure 5.1, 5.2 and 5.3 (right).

Subfigure (a) shows an exact agreement of the obtained tangential and sagittal curvature radii of the spherical mirror. This is expected as for spherical mirrors these are equivalent. This result can be seen as a good cross check for the analysis.

Subfigure (b) shows a behavior similar to the spherical mirror. This strengthens the conclusion drawn in the previous section that the cameras are moved during the calibration in a way that their observed surface element fits the model of a sphere which contracts the individual FPs.

In figure 4.6 the expected behavior for the measurement parameters  $u$  and  $v$  has been shown. Obviously, subfigure (c) fits the expectation for aspheres much better compared to (b) as sagittal and tangential FP are resolvable individually.

Table 5.1 shows the obtained curvature radii for the simulated aspherical mirror evaluated with a spherical reference mirror (fig. 5.6, c) together with those derived from the mathe-

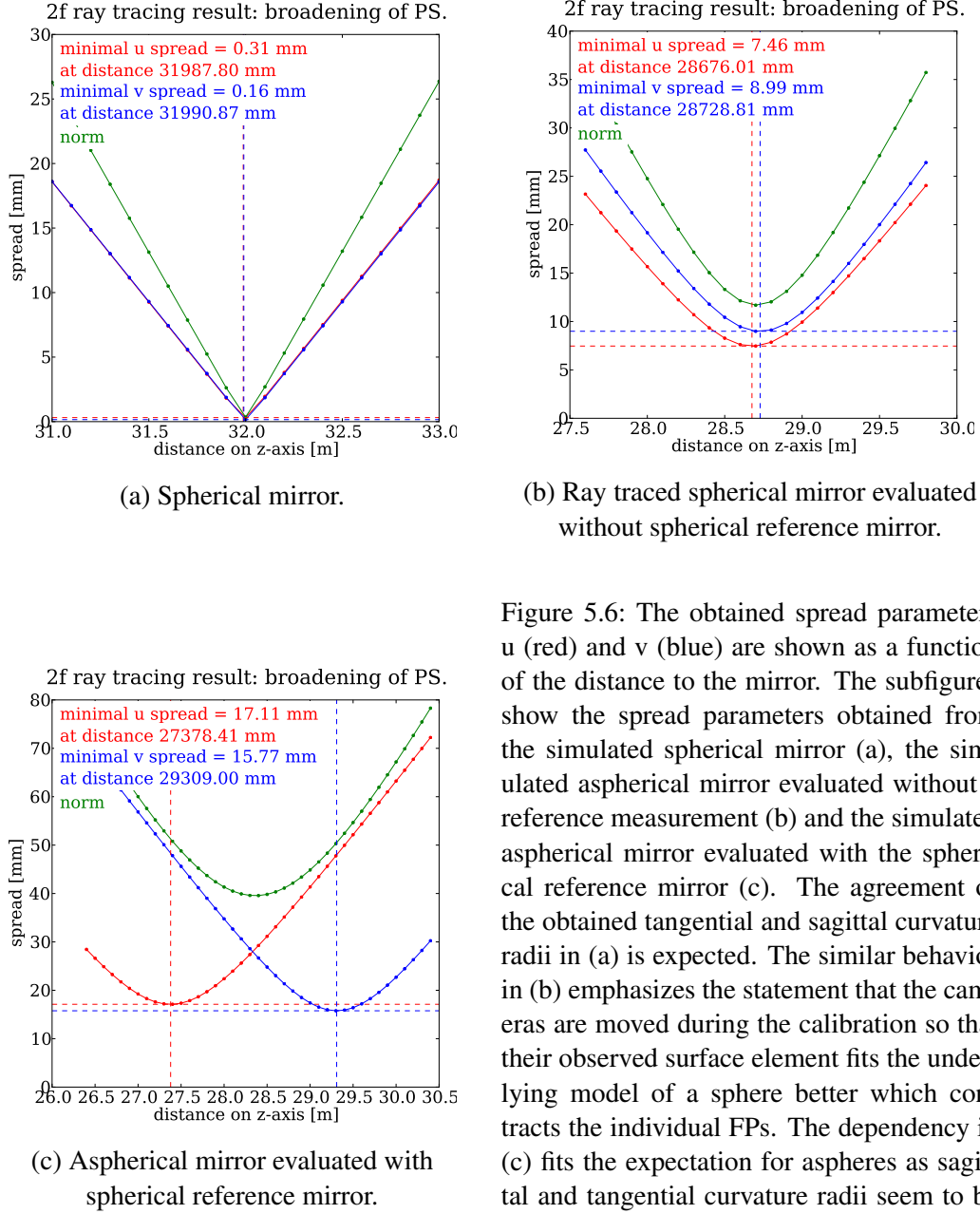


Figure 5.6: The obtained spread parameters  $u$  (red) and  $v$  (blue) are shown as a function of the distance to the mirror. The subfigures show the spread parameters obtained from the simulated spherical mirror (a), the simulated aspherical mirror evaluated without a reference measurement (b) and the simulated aspherical mirror evaluated with the spherical reference mirror (c). The agreement of the obtained tangential and sagittal curvature radii in (a) is expected. The similar behavior in (b) emphasizes the statement that the cameras are moved during the calibration so that their observed surface element fits the underlying model of a sphere better which contracts the individual FPs. The dependency in (c) fits the expectation for aspheres as sagittal and tangential curvature radii seem to be resolved. The corresponding PSFs at the obtained positions can be found in figure 5.1, 5.2 and 5.3 (right) respectively.

curv. radius	ideal mirror	PSF scanning
sagittal (here u)	26.36 m	27.38 m (+3.87 %)
tangential (here v)	29.18 m	<b>29.31 m</b> (+0.45 %)

Table 5.1: Obtained curvature radii from the measured ideal aspherical mirror. They are compared to those determined from the ideal mirror (see table 4.1). The tangential curvature radius can be resolved. The sagittal curvature radius is far beyond a reasonable value.

matical surface description determined in chapter 3.4. Remarkable is the observed deviation of the sagittal curvature of +3.87 %. The value of 27.38 m is out of the range of curvatures occurring (see ch. 3.4). The determination of the sagittal curvature radius is more inaccurate than of the tangential curvature radius because the sagittal curvature radii extend over a wider range of the o. a. That may be one reason for the observed deviation. Additionally there seems to be a systematics inside. The ray traced images clarify that statement. Figure 5.7 shows several PSs from the 2f ray tracing at distances near the sagittal curvature radius of the aspherical mirror. Noticeable is an odd region in the middle of the PSs which seems to spread the sides of the PSs apart. Taking only the spreaded edges of the PSs into account, the in chapter 3.4 determined sagittal curvatures, both the range and the minimal spread, can be vaguely perceptible at the obtained distances to the mirror. At distance 25.60 m to the mirror, the beginning of the sagittal curvature radius range can be recognized (compare to 25.78 m from figure 3.4, ch. 3.4). In the absence of the odd region the two spikes at the bottom should meet each other. At distance 26.80 m the end of the sagittal curvature radius range can be recognized (compare to 26.95 m from figure 3.4, ch. 3.4). The snapshot PS at distance 26.2 m relates to the distance with the minimal u value obtainable from the ideal surface (compare to 26.18 m from table 4.1, ch. 4).

The PSs show the expected behavior but are deformed by an unknown reason. A plausible candidate for the origin of the deformations are falsely determined slopes with PMD. For the PSF ray tracing two things are needed: a model for a surface representing the mirror and the via PMD obtained slopes. The small surface height deviation of around  $\pm 320 \mu\text{m}$  between the used spherical model and the asphere (see ch. 3.5) is too small to deform the PSs in the ray tracing to the observed extend. Therefore the slopes in the related region on the mirror have obviously been determined by far too flat while the ones at the edges seem to fit the expectation. Flatter slopes induce larger focal lengths and a widening of the PS in a fixed plane and hence can cause the observed effect. Therefore, the observed systematics is rather likely related to the process of the slope determination. It is conceivable that, indeed, the used spherical surface model is an incorrect, simplifying assumption which might be the origin of the observed broadening of the PSs.

Under this assumption one would also expect the tangential curvature to be not correctly resolvable. So far, the examination of the PSs shows that the identification of the tangential

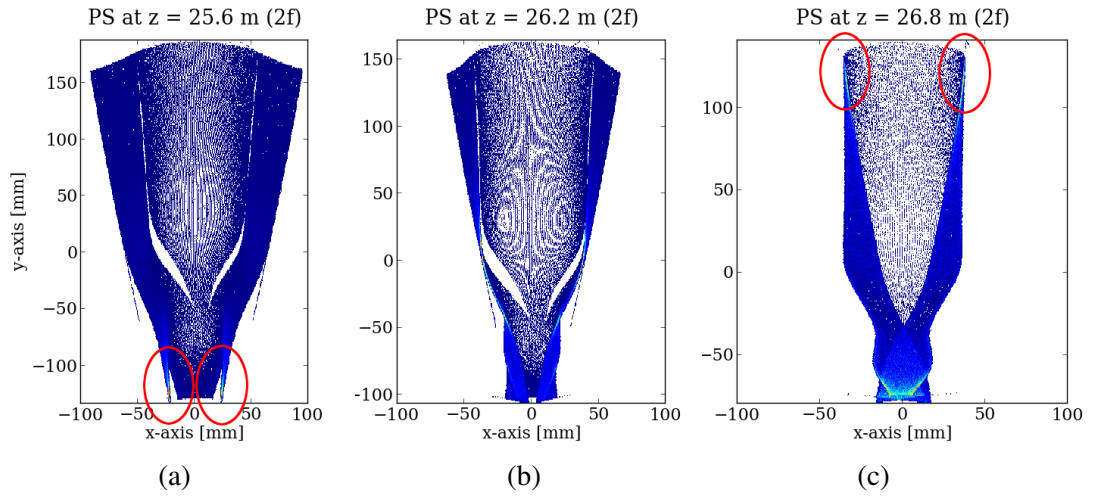


Figure 5.7: PSs from the 2f ray tracing at distances close to the sagittal curvature radius of the aspherical mirror. Shown is the PS of different scan plane along the optical axis. The beginning of the sagittal curvature radius range (beginning intersection at the bottom) can be seen in (a) and its ending (last intersections at the top) can be seen in (c). The PS in (b) is obtained near the distance with the minimal spread value  $u$  obtainable from the ideal surface (see chapter 3.4). Noticeable is the odd region occurring in the middle of every PS which seems to spread the sides apart. The markers highlight the focused parts of each PS which should meet in the absence of the underlying systematics.

curv. radius	ideal mirror	PSF scanning	PSF scanning (orthogonal)
sagittal	26.36 m	27.38 m (+3.87 %)	<b>26.32 m</b> (−0.15 %)
tangential	29.18 m	<b>29.31 m</b> (+0.45 %)	28.38 m (−2.74 %)

Table 5.2: Obtained sagittal and tangential curvature radii for two mirror orientations compared to those determined from the ideal mirror (see table 4.1).

curvature works quite well while there are problems with the determination of the sagittal curvature.

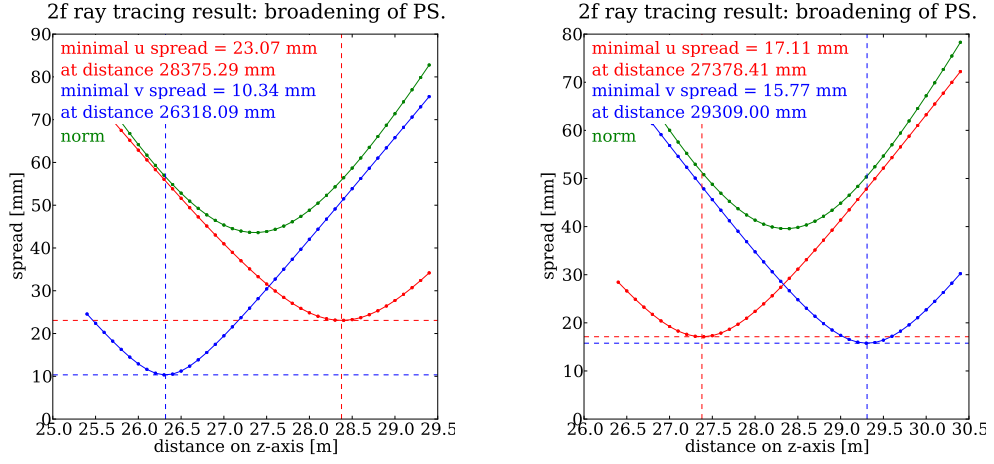
**Orthogonal mirror placement** Placing the aspherical mirror in the simulation orthogonal to the previous version (see figure 5.5) changes the measurement results. The sagittal curvature radius can now be determined but no longer the tangential curvature radius. The discussed odd region observed in the PSs occurs as above in the x-direction of the slopes.

The question is why the odd region in the PSs does not change its orientation with the mirror. It could be possible, that its origin might only be partly related to the used spherical surface model but is also connected to the camera parameters in the setup. It seems like there is a major systematics existing in the determination of the slopes along the setups x-direction: the used measurement setup is build with four cameras arranged in two pairs ((1, 4) and (3, 2)). Each two cameras of a pair have the same z-distance to the mirror plane and to the screen (y). Both cameras of a pair are arranged in the way to look on the mirror from the left (cameras 1, 2) respectively from the right (cameras 3, 4). The odd slopes appear exactly in the transition from the cameras 1, 2 to the cameras 3, 4. However, this effect can not be seen in the evaluation of spherical mirrors. During ray tracing their PSs show no similar patterns.

The odd region in the PSs occurs for mirrors measured in both placements and affects the spread along an axis independently of the mirror orientation. This seems to imply that the assumption of an underlying spherical surface model for measuring aspheres does not harmonize in combination with the chosen camera parameters of the PMD measurement setup. The curvature of aspheres might be too inhomogeneous that the cameras measure different slopes in their overlapping FOV and an adequate merging of the obtained slope data is not possible even if the final image seems to be merged astonishingly well.

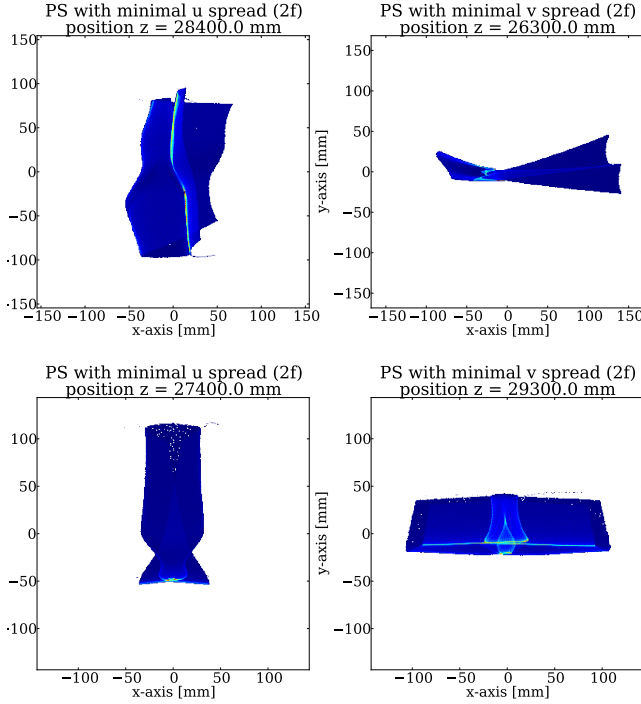
**Combination** The result of the evaluated and ray traced aspherical mirror placed orthogonal to the previous one including the distribution of the PS parameters  $u$  and  $v$  and the corresponding PSF at the minimal  $u$  and  $v$  can be seen in figure 5.8. They are shown together with their already presented counterparts of the commonly placed mirror. Table 5.2 shows the obtained curvature radii and those from the commonly placed counterpart.

In summary, the obtained slopes along the setups x-axis undergo a systematics which strongly limits their amount of information. The slopes obtained along the setups y-axis



(a) Spread parameters  $u$  and  $v$  as a function of the distance to the orthogonally placed mirror (b). Best-fit sphere radius was 27.10 m.

(b) Spread parameters  $u$  and  $v$  as a function of the distance to the commonly placed mirror (same fig. as 5.6, c). Best-fit sphere radius was 28.66 m.



(c) PS with minimum spread for the orthogonally placed mirror (a).

(d) PS with minimum spread for the commonly placed mirror (b).

Figure 5.8: Spread parameters of the PSs obtained during ray tracing (a,b) and the corresponding PSs with minimal  $u$ - and  $v$ -spread (c,d). The results from the asphere placed common (b,d) and orthogonal (a,c) are shown. It can be seen that only the slopes in  $y$ -direction result during a ray tracing in valuable PSs. These PSs meet the expectations for the asphere. The slopes in  $x$ -direction undergo a systematics that worsens the ability of evaluation.

are less affected by a similar systematics. With the combination of both measurements, the common one and the corresponding orthogonal one, it seems to be possible to measure both curvature radii of the aspherical mirror up to an accuracy of 0.5 % (see table 5.2).

It is conspicuous that if the best-fit radius of the spherical surface model was determined to be close to a curvature radius of the mirror, this curvature radius could be determined in the mentioned accuracy while the other could not.

### 5.3 Other methods of mirror quality analysis

Analyzing the curvature radii of an asphere is one method to characterize the mirrors quality. Another measure is its surface slope deviation relative to the underlying surface model. This is a measure typically used for spherical mirrors and can also be analyzed for aspherical mirrors. In addition, based on the obtained slopes, the real surface can be reconstructed by integrating over the slopes. Based on that result, also the height deviation relatively to the underlying surface model can be analyzed. All listed measures give information about the quality of a single mirror facet without the use of its counterpart. How these measures are obtained in the case of aspherical mirrors will be explained in the following.

Note that all the following analysis builds on the slopes obtained via the PMD evaluation. In the light of the observed systematics in the slope determination one has to keep in mind that this issue will automatically affect all the following results. Nevertheless, the presented techniques of characterizing the aspherical mirror give a rough impression about its surface quality and might be adequately applicable in the future. In addition, the discussion can also be focused on the data obtained from the axis which is less affected by the observed systematics.

#### 5.3.1 Surface reconstruction

In order to calculate deviations from the perfect surface height, the measured surface has to be reconstructed from the calculated slopes first. During the slope determination some of the data points might be filtered out. This happens during the procedure of cutting out irrelevant data in the area measured but not covered by the mirror. Filtered out data inside the mirror area is hindering the reconstruction of its surface and has to be restored. This is done via interpolating their few next neighbors in-line.

In order to fully reconstruct the mirror surface a starting point is chosen. This point is chosen to be in a location of the mirror where a maximum of data is available in both directions of reconstruction. Beginning at this starting point, the slopes in x-direction are used to create a two dimensional spline. Afterwards, from every point of the spline, the slopes in y-direction are integrated in order to reconstruct the full mirror surface. Figure 5.9 shows the originating slopes and the resulting reconstructed surface of a measured ideal aspherical mirror.

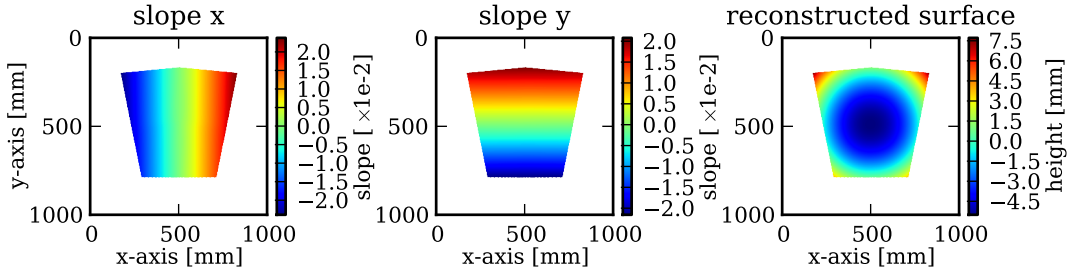


Figure 5.9: Based on the slope data (left) the mirror surface (right) can be reconstructed by integrating over the slopes.

In order to calculate slope as well as height deviations, the reconstructed surface has to be aligned to its describing aspherical surface model as good as possible. This is done via a sequence of multiple iterative fits that each minimize the height difference between the model and the reconstructed surface.

The surface is reconstructed from the slopes. As the slopes obtained for the aspherical mirror are affected by the systematics described above, the reconstructed surface will also be influenced.

### 5.3.2 Height deviation

Having aligned the measured surface and the exact surface model which can be derived from the formulas in chapter 3.3, these can be subtracted. The remaining height distribution represents the height deviation of the measured surface to its underlying model. The resulting height deviation for the simulated aspherical mirror to its surface model can be seen in figure 5.10.

The mirror surface could be reconstructed up to an accuracy of roughly  $\pm 100 \mu\text{m}$ . Conspicuous are the four lowerings and elevations in the surface height connected to the corresponding FOVs of the four cameras in the simulation. It seems that every camera measures a lowering or elevation at the middle of its FOV. These add up to the shown image. These lowerings and elevations could in contrast also represent the correct surface while the edges and the bump in the middle distort the alignment fit but a homogeneous radial structure originating in the four lowerings can be recognized which does not fit to the perfect surface. This result enforces the assumption that the curvature of aspheres might be too inhomogeneous to enable an adequate determination and merging of the obtained slope data for every camera.

The lowerings and elevations seem to have their origin in the already described systematics during slopes determination. Their distribution follows the position of the cameras in the setup and is independent of the mirror orientation. This fits to the observed effect that in both mirror placements one fixed direction of the slopes is affected by the systematics.



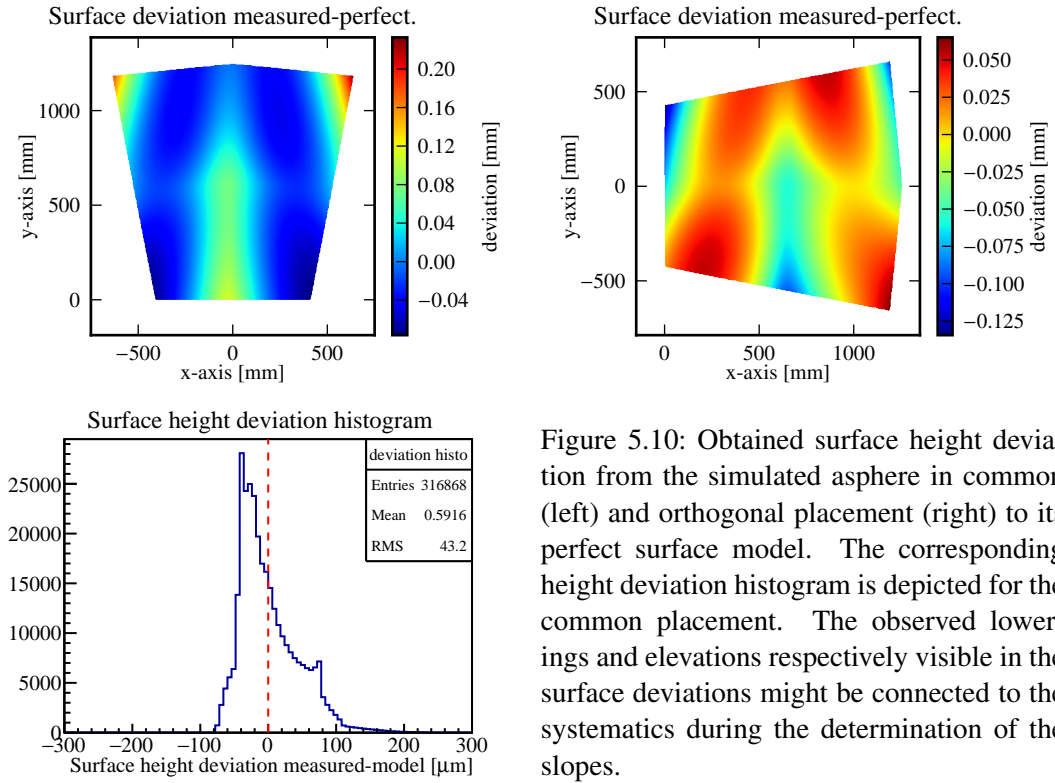


Figure 5.10: Obtained surface height deviation from the simulated asphere in common (left) and orthogonal placement (right) to its perfect surface model. The corresponding height deviation histogram is depicted for the common placement. The observed lowerings and elevations respectively visible in the surface deviations might be connected to the systematics during the determination of the slopes.

As explained in chapter 2 surface height and slope are connected to each other. The surface of an asphere and its best-fit sphere differ to maximal  $\pm 320\text{ }\mu\text{m}$ . Therefore, assuming the surface to be spherical will indeed influence the determination of the slopes at small scales as observed here.

Additionally the bump in the lower part of the mirror illustrates the property of the obtained surface data that is responsible for the odd region in the ray traced PSs shown above.

Furthermore, as described in Knauer (2006), the global accuracy of PMD is not high enough to enable a direct comparison of two edges of a measuring field. It is said, that the larger distance of surface and screen at the edges of the FOV may worsen the measurement result.

Looking at the histogram showing the surface height deviation data (see figure 5.10) offers another possibility of interpretation. The huge peak in the negative deviation regime corresponds to the blue area in the corresponding colorplot. The second peak and the broad tail in the positive deviation regime describes the green and red area in the color plot. This is exactly the area which is responsible for the observed effect during the determination of the curvature radii. As the fit aligns surface and model so that the height deviation is minimal it is no surprise that the core of the data in the height deviation histogram is arranged around a surface height deviation of zero. The mean value of the height deviation histogram gives information about the question how good the fit was able to align surface and model. The RMS value instead offers a possibility to characterize the actual surface quality. However, the existing systematics limits its validity.

### 5.3.3 Slope deviation

Having aligned the measured surface and the model, their slopes can be compared. For both directions  $x$  and  $y$  the slopes are calculated for the model and the measured surface. A subtraction of the slopes of the model and the reconstructed surface yields the slope deviation.

Figure 5.11 shows the slope deviation of the simulated aspherical mirror. The slope deviation displayed in a single image for each direction can be merged in one graph showing the tendency of slope deviation in the  $xy$ -plane. This gives an indication about the global deformation of the reconstructed surface. The corresponding graph can be found in figure 5.12.

In the light of the discussed systematics in the process of the slope determination it is no surprise that the slopes in  $x$ -direction deviate much compared to the slopes in  $y$ -direction. The slope deviation in  $y$ -direction also offers a spatial pattern that implies that the slopes in  $y$ -direction are also affected by a similar systematics but at an order of magnitude smaller. The observed lines parallel to the  $y$ -axis in the slope deviation in  $x$ -direction are connected to the applied method of surface reconstruction: the initial point for the surface reconstruction is located exactly between the flanks of the mirror. A variation of the calculated slopes perpendicular to the direction of reconstruction may point out the individuality of every single pixel in the slope data. Small variations including noise are summed up and become

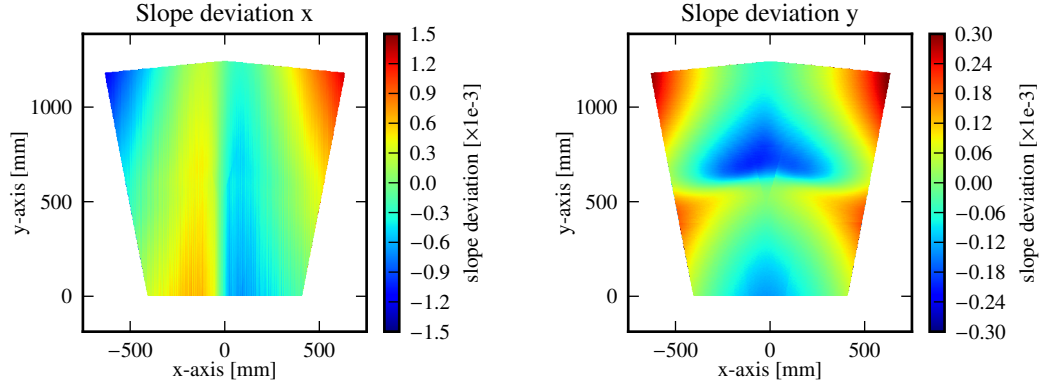
relevant. The increasing contrast in the slope deviation in x-direction (see figure 5.11) at points far away from the initial point emphasizes this assumption.

In summary, slope deviations of around  $\pm 1.2 \frac{\text{mm}}{\text{m}}$  (250 arcsec) for the sagittal curvature and around  $\pm 0.3 \frac{\text{mm}}{\text{m}}$  (60 arcsec) for the tangential curvature are observed. These values are near the limit of the PMD of around 150 arcsec given in Knauer (2006) and are a good result regarding the fact that the applied standard PMD evaluation uses an a priori deviating surface model.

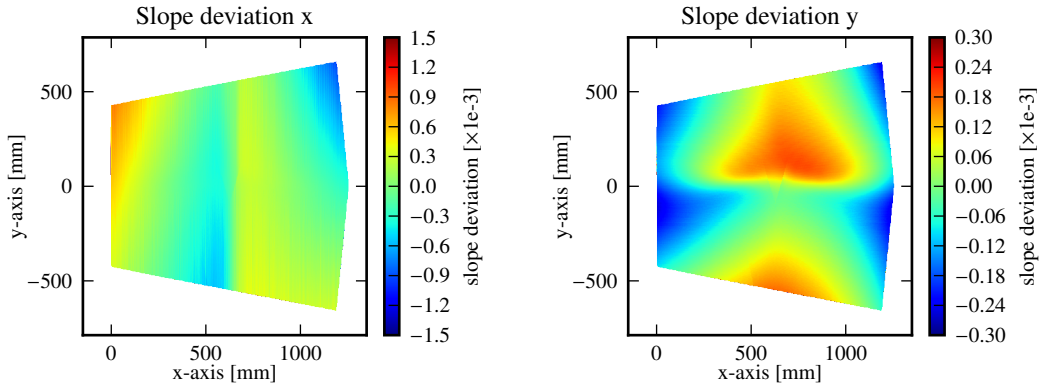
## 5.4 Discussion and conclusion

In this chapter it was attempted to measure aspherical telescope mirrors with the same approach used for measuring spherical mirrors. The assumption that the mirror can be described by a spherical surface was adopted. Practicable results can be achieved by measuring aspherical mirrors with a spherical reference mirror which is used to recalibrate the setup and enhance the measurement quality. The existing evaluation chain was adapted in an appropriate way. Based on the primary result of the PMD evaluation framework (the slopes) three possible ways of characterizing the measured aspherical mirrors quality have been studied: the analysis of the curvature radii, the analysis of the height deviation and the analysis of the slope deviation relative to the mirrors surface description. The curvature radii were obtained with a 2f analysis in a ray tracing: the optical axis was scanned for the minimum spread parameter values of u and v which define the ellipse covering the PS. Height and slope deviations were obtained by comparing the surface model and the aligned measured surface. Every characterization method has been applied to PMD measurements of an ideal P1 mirror.

These results show that the evaluation of aspherical mirrors with the standard PMD evaluation approach used for spherical mirrors, which includes the assumption that the measured surface can be described by a spherical surface model, is of limited suitability. It has been shown that the slopes belonging to the axis connecting cameras and screen (y-axis) are measured an order of magnitude more accurate than the slopes in the corresponding orthogonal axis connecting the cameras 1 and 4, and 2 and 3 (x-axis). More precisely, the amount of information obtainable for the global curvature in x-direction is reduced which only allows to analyze for local curvature deviations. This is not the case for the slopes in y-direction. This effect is very likely connected to the height deviation between the aspherical and the assumed spherical surface. As mentioned in chapter 2 the assumption of a known underlying surface structure is one way to solve the ambiguity in PMD. It was also explained that the slope of the surface determined with PMD is directly connected to the corresponding surface height. The surface height deviation between the measured aspherical surface and the describing spherical surface could therefore be the reason for the observed problems in the slope determination.



(a) Aspherical mirror measured in common placement.



(b) Aspherical mirror measured in orthogonal placement.

Figure 5.11: Slope deviation in x– (left) and y– (right) direction derived for the measured ideal aspherical mirror. In the light of the observed systematics in the slope determination it is not surprising that the slopes obtained along the setups x–direction deviate a lot while the slopes obtained along the setups y–direction do not. However, the spatial pattern of the slope deviation in y–direction shows evidence for a similar systematics but in an order of magnitude smaller.

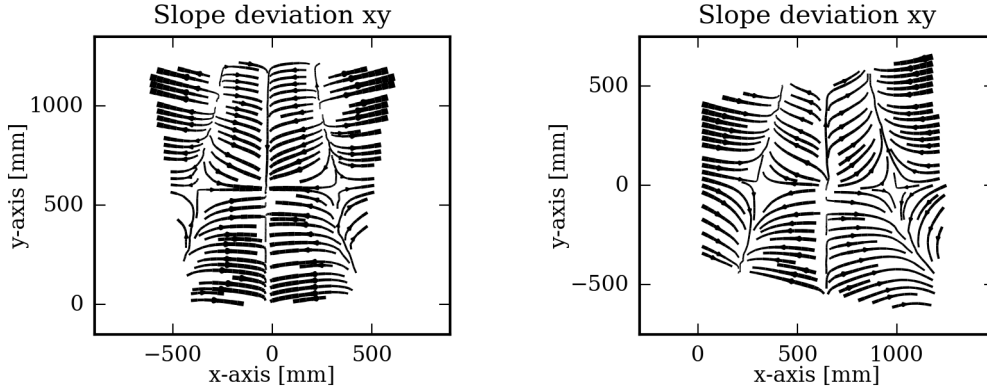


Figure 5.12: Combined view on the slope deviation for x- and y-direction in the form of a slope deviation tendency graph for the ideal aspherical mirror measured in its common placement (left) and its orthogonal placement (right). The four camera effect can be observed in both measurements.

The distance of the cameras to each other in y-direction is equal. The distance in x-direction is not equal for the two pairs of cameras (1, 4) and (2, 3). Conspicuous is the fact that the slopes measured in the direction where the distances of the cameras to each other are equal (y-direction) deviate relatively to the perfect slopes from the ideal P1 mirror an order of magnitude smaller compared to the slopes measured in the direction where the distances of the cameras to each other are not equal (x-direction). Taking the best-fit radius of the spherical model aligned to the measured aspherical mirror into account, it is noticed that the radius of the spherical model is more influenced by the surface curvature in y-direction of the measurement setup than in x-direction: for the mirror orientation in common placement, which means an alignment of the mirrors tangential curvature along the y-direction, best-fit sphere radii are obtained that are closer to the expected tangential curvature radius. For the mirror orientation in orthogonal placement, which means an alignment of the mirrors sagittal curvature along the y-direction, best-fit sphere radii are obtained that are closer to the expected sagittal curvature radius. The curvature of the mirror which was better approximated by the fitted spherical model could be reproduced in a ray tracing as explained above. The above results all induce that the assumption that the measured surface can be approximated by a spherical surface model is not ideal for measuring aspherical mirrors and point out that the surface model alignment is more affected by the slope data in y- than in x-direction.

A possible improvement could therefore be achieved by a measurement setup where the cameras have the same distances at the edges. An alternative approach might be the introduction of a fifth camera which is located between the cameras of the camera pair with the larger distance to each other (2, 3). As a result the slopes in x-direction might smooth and enhance the measurement result. The best possible improvement is most likely achieved by

the evaluation of the mirror with the use of the correct or at least a more suitable surface model.

The observed problem in the slopes determination affects all results of the further analysis. But, as shown, by measuring the aspherical P1 mirror in two orthogonal orientations both curvature radii can be obtained up to an accuracy of 0.5 %.

## 6 Application to the mirror facet P1.016 from the prototype Schwarzschild–Couder Telescope

The systematics of the PMD measurement in the context of measuring aspherical mirrors has been studied in the last chapter by measuring an ideal aspherical P1 mirror. In this chapter the PMD measurement is applied to a real version of the P1 mirror.

For testing purposes, there was a mirror facet of type P1 at ECAP. The facet was built for a prototype medium sized SCT and was labeled as P1.016 (see figure 6.1). P1.016 is a mirror element from the inner ring of the primary telescope mirror. Its size is about 1.25 m from the bottom to the tip and about 1.31 m between the flanks. The reflecting surface features an interesting distortion in the middle of the mirror which can be noticed by the naked eye and is clearly detectable in the following analysis.

### 6.1 Determination of curvature radii and focal planes

In order to verify the results obtained via the PMD evaluation method, a reference measurement using the so called 2f method is carried out. The 2f measurement is described in detail in Wörnlein (2012). In the following the results obtained from the 2f method are shown.

#### 6.1.1 2f measurement

If a light source is positioned exactly in the distance of twice the focal length of a reflecting surface (2f distance) its light will be reflected and focused exactly in the position of the light source. The classical setup of a 2f measurement is depicted in figure 6.2.

The 2f measurement is carried out as follows: in order to obtain the curvature radii of the asphere, the distance of the light source and the camera to the mirror is varied until a minimal u and v spread was found. The distances of these two points are equal to the curvature radius of the axes. The obtained curvature radii of the aspherical mirror can be found in table 6.1. The range of sagittal curvature radii was found to extend from 25.69 m up to 26.60 m.

The tangential curvature radius was measured close to the expectation. A reason for the deviation in the obtained sagittal curvature radius could be the fringe which can be seen in figure 6.3 (left). The intense buckle in both PSs is caused by the distortion of the mirror surface. Due to this deformation of the PS the sagittal curvature radius determination may be strongly influenced.

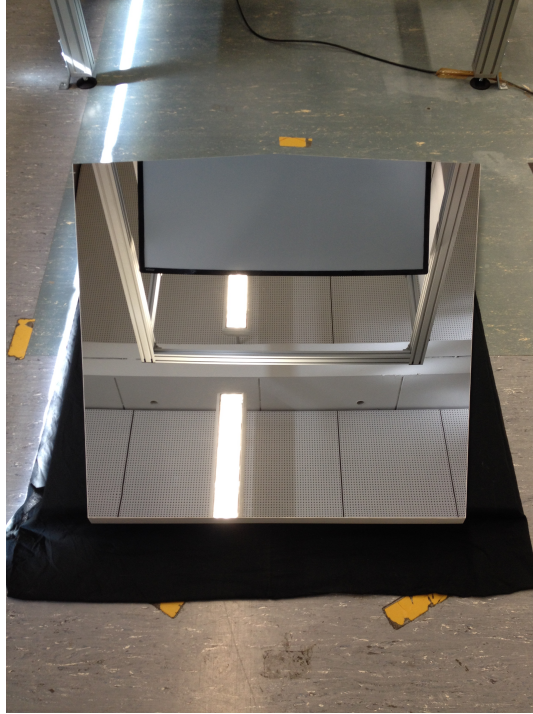


Figure 6.1: Aspherical mirror facet P1.016 of a prototype medium sized SCT. P1.016 is a mirror element from the inner ring of the primary telescope mirror.

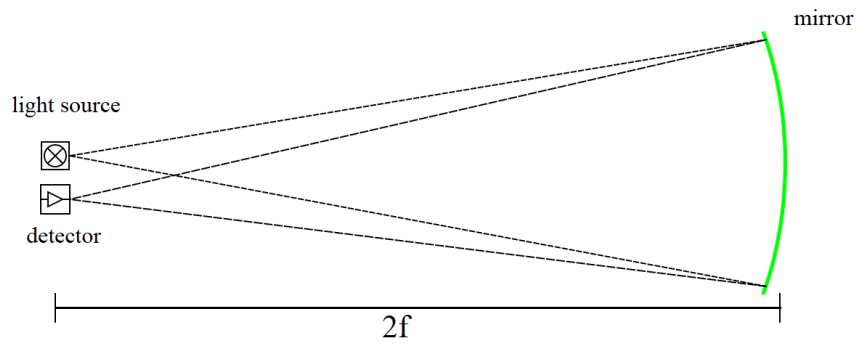


Figure 6.2: Classical  $2f$  measurement setup. A light source and a camera are at the same distance to a reflecting surface (image from Schulz 2010).



curv. radius	ideal mirror	2f measurement
sagittal	26.36 m	26.30 m (−0.23 %)
tangential	29.18 m	29.16 m (−0.07 %)

Table 6.1: Curvature radii determined by a 2f-measurement of the P1.016 mirror together with those determined from the ideal P1 mirror.

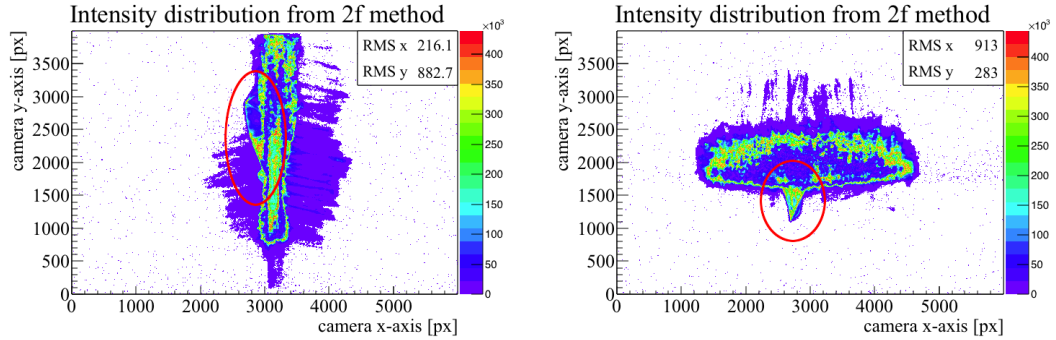


Figure 6.3: 2d intensity distributions of the pictures taken during the 2f measurement representing the PSFs. Shown are the PSFs near the obtained minimal u (left) and v (right) spread values. Distinct buckles are marked.

### 6.1.2 PMD measurement

By measuring the aspherical mirror in the common and in the orthogonal placement both curvature radii are obtainable via a standard PMD measurement as discussed in the previous chapter. Table 6.2 shows the obtained tangential and sagittal curvature radii and those obtained with the 2f measurement. Figure 6.4 shows the corresponding PSs with the minimal spreads u and v.

The curvature radii obtained from PMD are more than 1 % larger than those obtained with the 2f measurement. In the last chapter, it was derived that the curvature radii can be measured up to an accuracy of around 0.5 %. This was the case for ideal aspherical mirrors. As the results from the real mirror show stronger deviations it can be inferred that surface irregularities strongly affect the PMD evaluation of aspherical mirrors with the technique

curv. radius	2f measurement	PMD measurement
sagittal	26.30 m	26.59 m (+1.10 %)
tangential	29.16 m	29.61 m (+1.54 %)

Table 6.2: Obtained curvature radii from the PMD measured aspherical mirror P1.016 in combination to those determined with the 2f measurement.

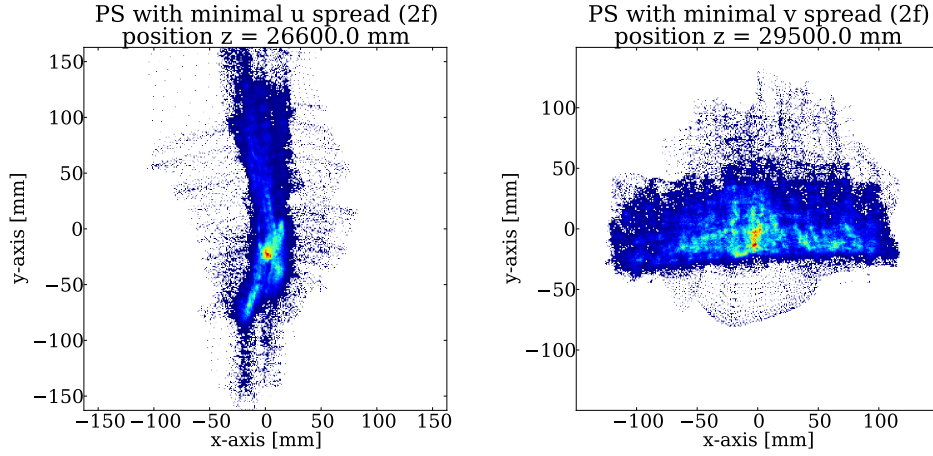


Figure 6.4: Ray traced PSs from scan planes close to the positions with minimal  $u$  and  $v$  values. The bulge in the minimum  $v$  PS is caused by a strong local deformation in the middle of the mirror surface.

used for spherical mirrors. The mirror features a strong local deformation in its middle which of course is not advantageous in the sense of aligning a spherical model to a surface which is already by definition not perfectly describable by a sphere.

## 6.2 Height deviation

Having reconstructed the surface from the measured slopes the height deviation of the measured surface relative to its mathematical description can be calculated. Figure 6.5 shows the spatially resolved surface height deviation and the corresponding histogram. As mentioned before the RMS of the surface height deviation histogram can be understood as an indicator for the mirror quality. In the light of the observed problems in the slope determination process the absolute RMS value is less conclusive but comparable to the one obtained from the analyzed simulated aspherical mirror. With a value of  $50.32\,\mu\text{m}$  the reconstructed surface has a RMS that is about  $7.12\,\mu\text{m}$  higher (around +17 %) compared to the simulated one. The yellow dot in the mirror corresponds to the already mentioned local deformation of the mirror surface.

## 6.3 Slope deviation

The deviation of the measured slopes relatively to those from the ideal P1 mirror can be computed.

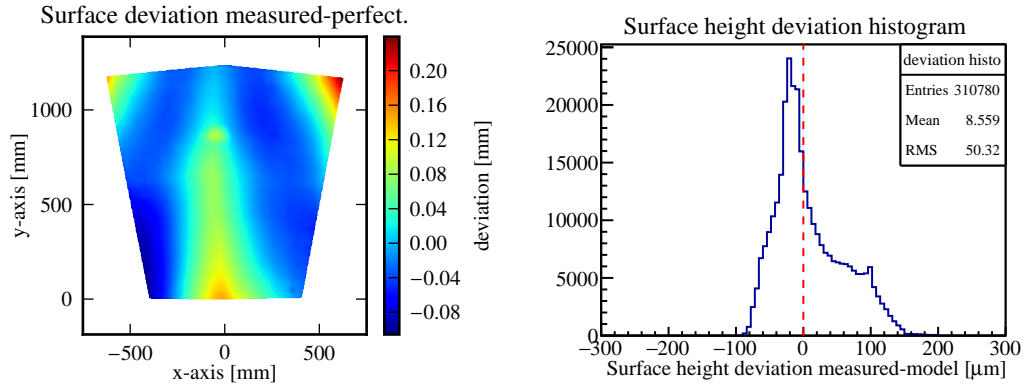


Figure 6.5: Spatially resolved surface height deviations between reconstructed surface and surface model (left). The corresponding histogram (right) is shown. The dot in the middle of the mirror corresponds to a local deformation of the real mirror surface. The RMS of the height deviation is about 17 % higher compared to the measurement of the ideal mirror.

The slope deviation in  $y$ -direction shows grooves that might be a consequence of the production process of the mirror facet. Compared to the slope deviation tendency of the measured ideal aspherical mirror (see fig. 5.12) the one derived for the real mirror presented in figure 6.7 is expectedly less homogeneous. It also shows the strong local deformation inside the mirror and larger deviations at the mirrors edge.

## 6.4 Conclusion

In this chapter the aspherical mirror P1.016 was measured with PMD using the assumption that the mirror surface can be described by a spherical surface model. As explained, the mirror had to be measured in two orientations like explained in the last chapter.

The mirrors curvature radii were determined via the PMD evaluation to 26.59 m and 29.61 m. Compared to the reference values obtained with the  $2f$  measurement these radii are +1.10 % and +1.54 % larger. As the results show stronger deviations than those determined from ideal aspherical mirrors and the P1.016 mirror features a strong local deformation in its middle it can be inferred that surface irregularities strongly affect the PMD evaluation of aspherical mirrors with the technique used for spherical mirrors. It could be shown that the surface height deviates around +17 % worse compared to a corresponding analyzed ideal aspherical mirror. The slope deviation is large at the edges of the mirror and shows various grooves inside the mirror which might be a consequence of the production process of the mirror facet.

The strong local deformation of the mirror surface could clearly be resolved during the analyses. Also smaller local deformations could be identified which are caused by spacers

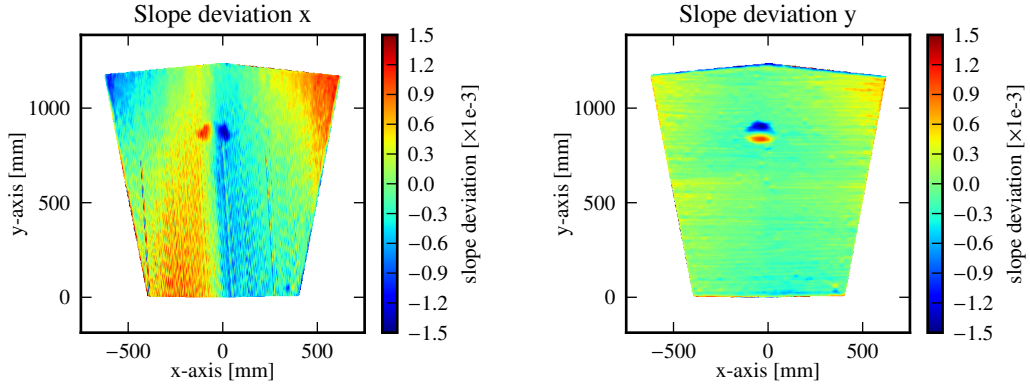


Figure 6.6: Calculated slope deviation in directions x (left) and y (right). Artifacts caused by the surface reconstruction (compare ch. 5.3.3) manifest as stripes and are visible in the x–slope deviation. The dots in the mirrors middle correspond to a local deformation in the mirrors surface. Smaller point–like local deformations are visible particularly in the bottom right.

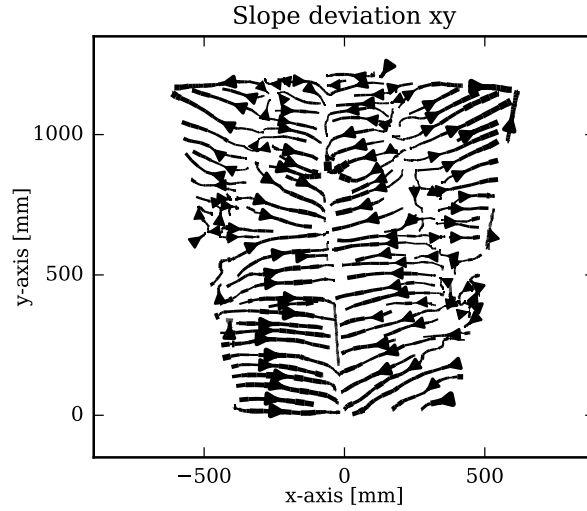


Figure 6.7: Slope deviation tendency graph showing the combined slope deviation for x– and y–direction. Compared to the slope deviation tendency of the measured ideal aspherical mirror (see fig. 5.12) the corresponding one of the measured P1.016 mirror is of course less homogeneous. Visible is the strong local deformation inside the mirror and larger deviations at the mirrors edge.

mounted on the backplane of the mirror which push through the mirror and locally deform it.

## 7 Measuring aspherical mirror facets with an ellipsoidal surface model

The results of the last chapters clearly show that the standard way of measuring telescope mirrors with PMD under the assumption that the surface under test can be described by a spherical surface model is not ideal for the application to aspherical mirrors. As the used aspheres have two different curvatures the result of the evaluation strongly depends on the alignment of the spherical surface model. It is conspicuous that the curvature radius closer to the best-fit radius of the describing spherical model was reconstructed with smaller deviations compared to the other one.

A shape that might provide a better approximation of the aspherical mirror surface with its two individual curvatures could be a rotationally symmetric prolate ellipsoid (see fig. 7.1 for illustration) which provides two different curvature radii. Therefore, this chapter is focused on the question whether or not the analyses discussed in the last chapters could be enhanced by replacing the spherical surface model by the ellipsoid.

In order to answer that question the PMD evaluation was modified to use the rotationally symmetric prolate ellipsoid as the underlying surface model. Based on this new approach it is tried in the following to determine the curvature radii of an ideal P1 mirror and of the real P1.016 mirror. Surface height and slope deviation are calculated and analyzed based on this new approach.

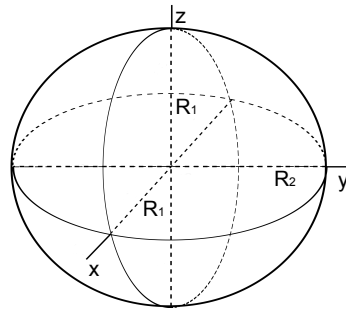


Figure 7.1: Illustration of the model of a rotationally symmetric prolate ellipsoid. This shape features two curvature radii  $R_1$  and  $R_2$  with a rotational symmetry along the y-axis.

curv. radius	ideal mirror	PMD sphere	PMD ellipsoid
sagittal	26.36 m	26.32 m (−0.15 %)	<b>26.49 m</b> (+0.49 %)
tangential	29.18 m	29.31 m (+0.45 %)	<b>29.32 m</b> (+0.48 %)

Table 7.1: Curvature radii from the ideal aspherical P1 mirror measured with the new ellipsoidal approach together with those determined directly from the ideal P1 mirror and those obtained with the standard spherical approach (compare ch. 5) from both measured placements.

curv. radius	2f	PMD sphere	PMD ellipsoid
sagittal	26.30 m	26.59 m (+1.10 %)	<b>26.66 m</b> (+1.37 %)
tangential	29.16 m	29.61 m (+1.54 %)	<b>29.22 m</b> (+0.21 %)

Table 7.2: Curvature radii from the aspherical P1.016 mirror measured with the new ellipsoidal approach together with those measured in the 2f measurement and those obtained with the standard spherical approach (compare ch. 6) from both measured placements.

## 7.1 Curvature Radii of the ideal aspherical mirror

In a first approach the curvature radii of the ideal aspherical P1 mirror which was already measured in chapter 5 are determined with the new ellipsoidal approach. For this purpose only the dataset in common placement was used. Having calculated the slopes using on the ellipsoidal surface model the curvature radii can be determined by a ray tracing as described in the last chapters.

Table 7.1 shows the obtained tangential and sagittal curvature radii together with those determined directly from the ideal P1 mirror and those obtained from the previous evaluation using the spherical model. Both curvature radii were determined from just one single measurement up to an accuracy of below 1 %. It seems like the approach with the ellipsoidal surface model slightly overestimates the curvature radii. Compared to the radii obtained in chapter 5 this approach seems to gain a worse accuracy.

Figure 7.2 shows the dependency of the spread parameters  $u$  and  $v$  on the distance to the mirror and figure 7.3 shows the corresponding PSs with the minimal spreads  $u$  and  $v$ . The PSFs for tangential and sagittal curvature are reproduced better than using the spherical PMD evaluation approach (compare fig. 5.8).

## 7.2 Curvature Radii of the real aspherical mirror

The curvature radii of the real aspherical mirror P1.016 from chapter 6 are determined. Again only the measurement in common placement was used.

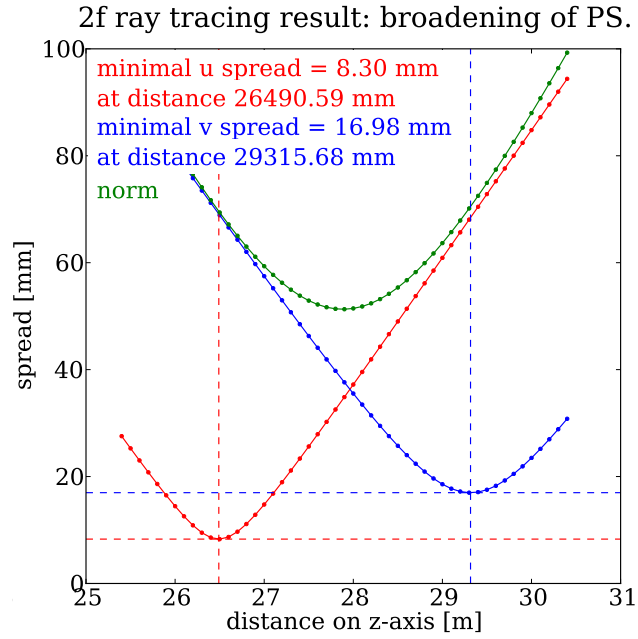


Figure 7.2: Simulated aspherical mirror: Dependency of the spread parameters  $u$  and  $v$  on the distance to the mirror. Both curvature radii can clearly be resolved from just one measurement. The best-fit ellipsoidal radii are 26.50 m and 27.86 m.

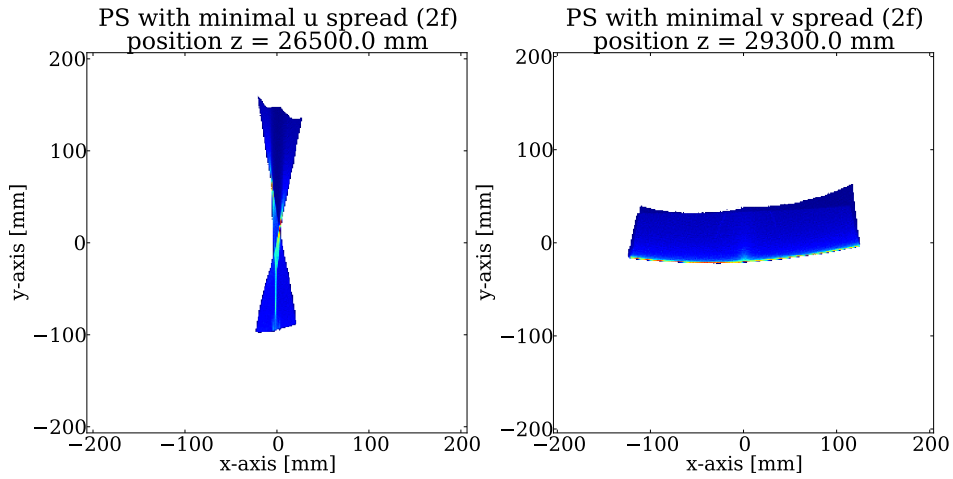


Figure 7.3: PSs of the simulated aspherical mirror from scan planes close to the positions with the minimal spread parameters  $u$  and  $v$  (minima in fig. 7.2).



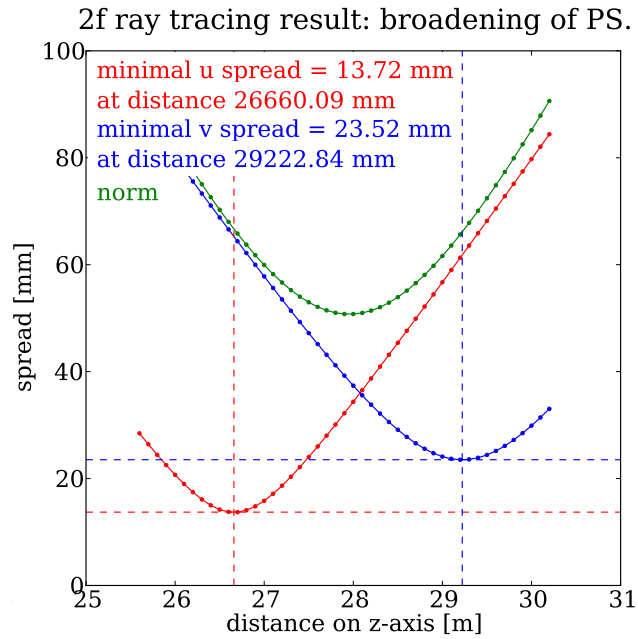


Figure 7.4: Measured P1.016: Dependency of the spread parameters  $u$  and  $v$  on the distance to the mirror. Again both curvature radii can clearly be resolved from just one measurement. The best-fit ellipsoidal radii were 26.79 m and 28.09 m.

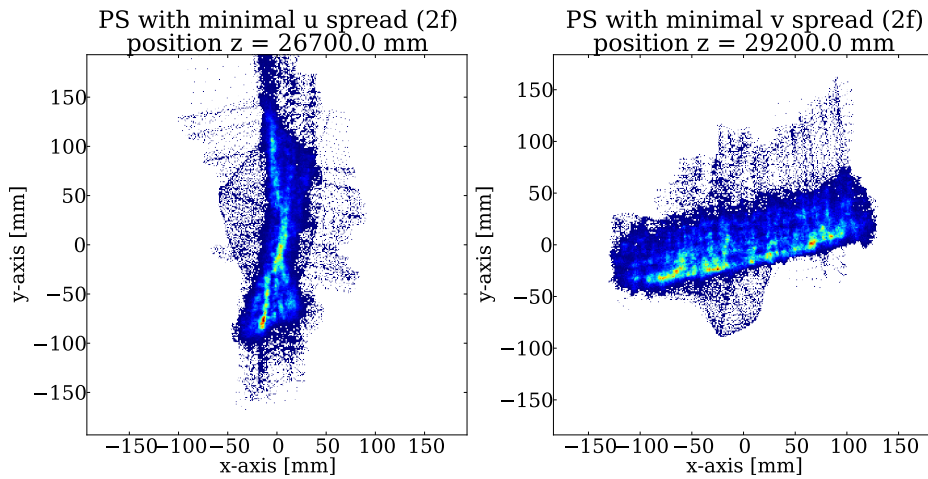


Figure 7.5: PSs of the aspherical mirror P1.016 from scan planes close to the positions with the minimal spread parameters  $u$  and  $v$  (minima in fig. 7.4).

Table 7.2 gives an overview of the obtained tangential and sagittal curvature radii and shows them together with those determined via the  $2f$  measurement and those obtained in the previous measurement using the spherical surface model.

Also for the real aspherical mirror both curvature radii were obtained from just one single measurement. The radii could be measured up to an accuracy of below 1.5 % compared to the value obtained from the  $2f$  measurement. The obtained value for the tangential curvature fits much better compared to the one derived using the spherical surface model in chapter 6 while the value for the sagittal curvature shows no strong difference.

Figure 7.4 shows the dependency of the spreads  $u$  and  $v$  on the distance to the mirror and figure 7.5 shows the corresponding PSFs with the minimal spreads  $u$  and  $v$ . The PSFs for tangential and sagittal curvature are reproduced astonishingly well compared to those obtained in the  $2f$  measurement (compare fig. 6.3).

### 7.3 Height deviation

Having reconstructed the surface from the measured slopes the height deviation of the surface under test relative to its mathematical description can be calculated. The obtained surface height deviation of the measured ideal P1 mirror and of the measured P1.016 mirror — both evaluated with the ellipsoidal approach — are shown in figure 7.6 and 7.7.

The lowerings and elevations which could be observed in the evaluation using the spherical surface model approach (see fig. 5.10) can not be seen here. The local deformation of the P1.016 mirror surface is clearly resolved. The surface height deviation for the ideal P1 mirror evaluated with the ellipsoidal surface model approach features a RMS value of  $26.1\text{ }\mu\text{m}$  which is about half of the RMS value obtained using the spherical surface model approach ( $43.2\text{ }\mu\text{m}$ , see fig. 5.10). The corresponding RMS value for the measured P1.016 mirror  $74.07\text{ }\mu\text{m}$  evaluated using the ellipsoidal surface model approach is larger than the obtained RMS value using the spherical surface model approach. The obtained mean values of the surface height deviation histograms for the ideal P1 mirror ( $0.11\text{ }\mu\text{m}$ ) and the P1.016 mirror ( $0.37\text{ }\mu\text{m}$ ) are much smaller compared to the ones obtained with the spherical surface model approach ( $0.59\text{ }\mu\text{m}$  and  $8.56\text{ }\mu\text{m}$ , see fig. 5.10 and 6.5).

### 7.4 Slope deviation

The deviation of the slopes determined from the measured ideal P1 and the measured P1.016 mirror relative to those from their mathematical description can be computed and are shown in figure 7.8 and 7.9. The  $x$ -slope deviation obtained for the ideal P1 and the P1.016 mirror shows artifacts caused by the surface reconstruction (compare ch. 5.3.3) manifesting as vertical stripes. The slope deviations in  $x$ - and  $y$ -direction show a gradient pattern which is rather likely connected to a systematics occurring in the PMD measurement using the ellip-

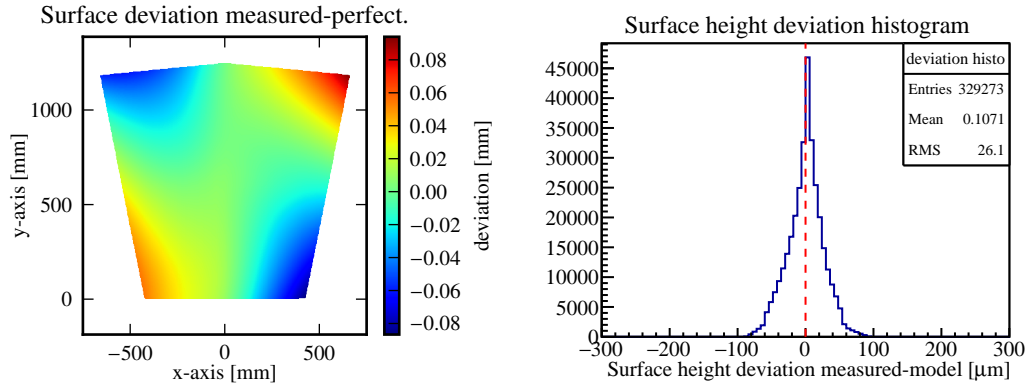


Figure 7.6: Surface height deviation of the measured ideal P1 mirror relative to its mathematical description spatially resolved (left) with the corresponding histogram (right).

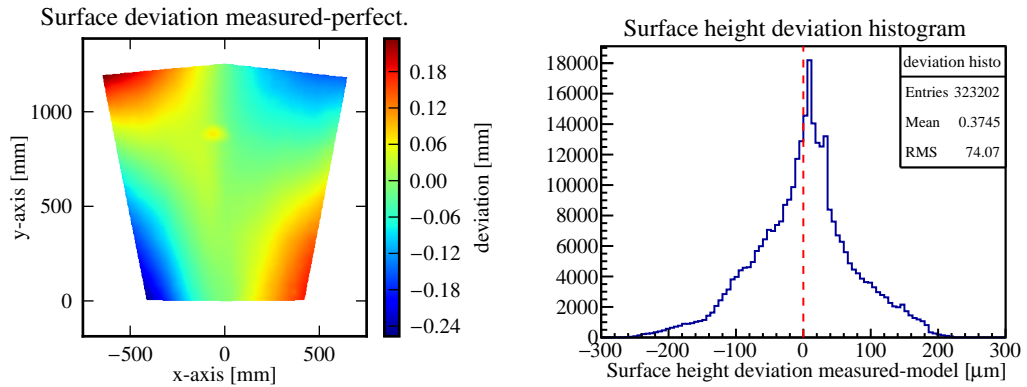


Figure 7.7: Surface height deviation of the measured P1.016 mirror relative to its mathematical description spatially resolved (left) with the corresponding histogram (right). The visible local deformation of the mirror surface causes a second peak in the histogram right next to the main peak.

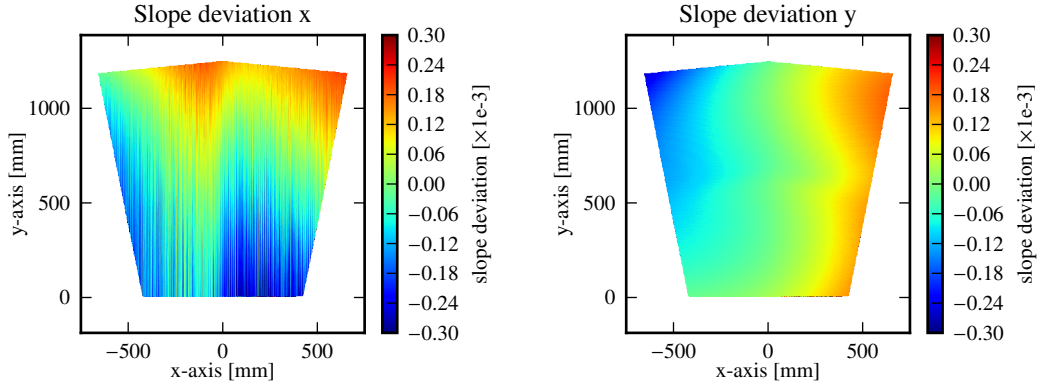


Figure 7.8: Calculated slope deviation in directions x (left) and y (right) of the measured ideal P1 mirror. Artifacts caused by the surface reconstruction (compare ch. 5.3.3) manifest as stripes and are visible in the x-slope deviation. The dots in the mirrors middle correspond to a local deformation in the mirrors surface. Smaller point-like local deformations are visible particularly in the bottom right.

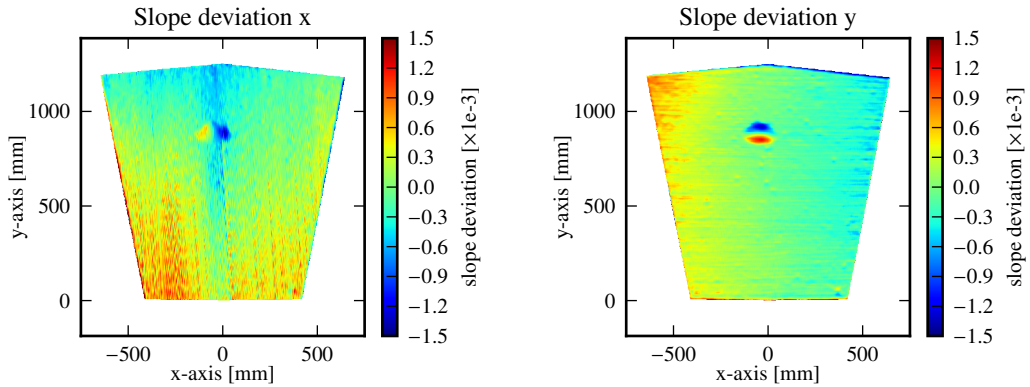


Figure 7.9: Calculated slope deviation in directions x (left) and y (right) of the measured P1.016 mirror. Artifacts caused by the surface reconstruction (compare ch. 5.3.3) manifest as stripes and are visible in the x-slope deviation. The surface properties observed with the standard spherical surface model approach are reproduced.

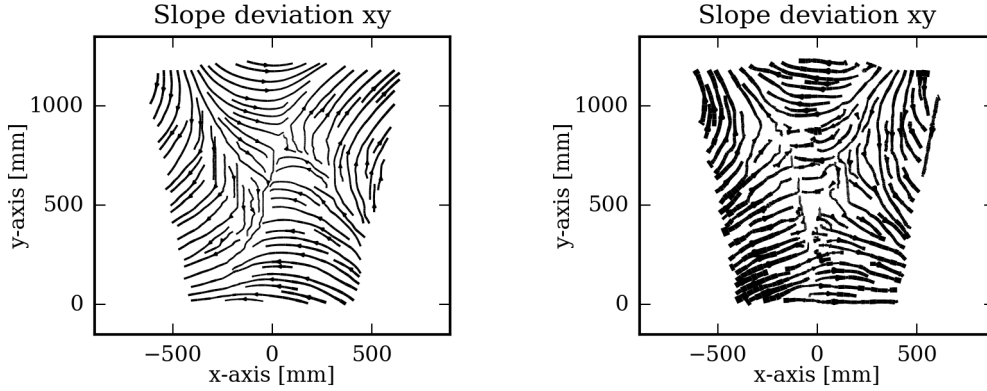


Figure 7.10: Slope deviation tendency graphs showing the combined slope deviation for x- and y-direction for the measured ideal P1 mirror (left) and the P1.016 mirror. Compared to the slope deviation tendency of the measured ideal P1 mirror (see left) the corresponding one of the measured P1.016 mirror is of course less homogeneous. Visible is the local deformation inside the mirror and larger deviations at the mirrors edges.

soidal approach. The mirror surface properties of the real P1.016 mirror observed in the last chapter (see fig. 6.6) are reproduced with the ellipsoidal approach.

The corresponding slope deviation tendency graphs for the P1 and the P1.016 mirror are shown in figure 7.10.

## 7.5 Discussion and conclusion

In this chapter an ideal and a real P1 aspherical mirror facet were measured with PMD under the assumption that the mirror surface can be described by a rotationally symmetric prolate ellipsoidal surface model. The advantage of this surface model is that it allows two different curvature radii which seems to provide a better approximation to the real aspherical surface structure than spherical surface models. It was analyzed whether the measurement results are enhanced by using the ellipsoidal surface model. In the course of that the curvature radii obtained from PMD measurements, the deviation of the reconstructed surface height and the obtained slope deviation were investigated.

Indeed with the surface model of an ellipsoid it is possible to obtain both curvature radii during ray tracing up to an accuracy of below 0.5 % for an ideal P1 mirror measured in just one orientation. By comparing the resulting values of the curvature radii it seems like the ellipsoidal surface model is more stable in the presence of surface irregularities than the spherical model. While the sagittal curvature radius could be obtained in a comparable quality the tangential curvature was measured much better compared to the evaluation technique used for spherical mirrors. A reason for the still deviating sagittal curvature radius could be

that the distortion of the PSs caused by the strong local deformation of the mirror surface result in a different determined minimal spread parameter. It is possible that also the ellipsoid is not a good enough approximation of the surface of aspherical mirrors.

Remarkable is the good reproduction of the effects visible in the PSs caused by the local deformation of the P1.016 mirror surface. These effects are clearly visible in the intensity distributions measured within the 2f measurement shown in figure 6.3 but not in the PSs obtained with the standard PMD evaluation shown in figure 6.4. This seems to be another qualitative statement that the ellipsoidal surface model is more suitable for the application in measuring aspherical mirrors than spherical surface models are.

The local mirror deformation is clearly resolved in the surface height deviation analysis. The lowerings and elevations which could be observed in the evaluation using the spherical surface model approach do not appear in the evaluation using the ellipsoidal surface model approach. Instead, the color structure of the surface height deviation plots (see fig. 7.6 and 7.7) implies that another systematics may be involved in the PMD measurement using the ellipsoidal approach. Its exact origin is still under investigation. A misaligned surface model during the evaluation step might be the reason for the observed patterns. The mean values of the corresponding surface height deviation histograms are much smaller than those obtained with the spherical surface model approach. The mean value gives information about how good the reconstructed surface and its describing model could be aligned. A smaller value implies a better alignment. The mean values obtained for the ellipsoidal approach are smaller than those obtained for the same mirrors using the standard spherical approach. This result implies that the existing alignment algorithm seems to work better with reconstructed aspherical surfaces that were created from slopes measured with the ellipsoidal approach. The RMS value of the surface height deviation histogram is a measure of the mirrors surface quality. As the RMS value obtained for the measured ideal P1 mirror using the ellipsoidal approach ( $26.1\text{ }\mu\text{m}$ ) is much smaller compared to the corresponding RMS value obtained by using the standard spherical approach ( $43.2\text{ }\mu\text{m}$ ) it can be concluded that the aspherical surface under test is measured more accurate with the ellipsoidal approach. Again, this result points out that the evaluation with the ellipsoidal surface model seems to be more appropriate for aspherical mirror facets than the standard evaluation with a spherical surface model. Unexpectedly, the RMS value obtained for the measured P1.016 mirror by using the ellipsoidal approach ( $74.07\text{ }\mu\text{m}$ ) is larger compared to the value determined for the same mirror by using the standard spherical approach ( $50.32\text{ }\mu\text{m}$ ). This behavior of the RMS might be due the fact that the surface is obviously measured worse with the standard spherical approach. This implies a systematically wrong measurement of the surface slopes and hence a wrong reconstructed surface height that eventually may be reconstructed to be more homogeneous that it actually is. This implies that the RMS value obtained with the standard spherical approach is measured as too small and might explain the larger RMS value obtained here. In contrast a misaligned surface model in the determination of the surface height deviation might also cause the observed distribution of the surface height deviation. The small mean value implies a good global alignment of the reconstructed surface and the mathematical surface

description but the mean value would not change in the presence of a tilt between both surfaces. Indeed a tilted surface could explain the determined large RMS value here. However the exact origin of the observed behavior of the RMS is currently under investigation.

The spatially resolved slope deviation shows a gradient pattern which is connected to the observed systematics in the surface height deviation. The mirror surface properties of the real P1.016 mirror observed in the last chapter (see fig. 6.6) are reproduced with the ellipsoidal approach.

Also remarkable is the smaller residual remaining in the positioning of the ellipsoidal surface model during the PMD evaluation compared to the spherical model: in chapter 2 it was explained that the ambiguity in PMD can be solved by determining the best-fit position and orientation of the underlying surface model. In order to obtain the best-fit position and orientation it is looked for a minimum in the discrepancy between the screen pixels got hit by the on the positioned surface reflected sight rays and the screen pixels that should be hit. The residual in the best-fit location of the ellipsoidal surface model is around 4 times smaller than the corresponding residual for the spherical surface model. This shows directly that the approximation of the aspherical surface by an ellipsoid matches much better than the spherical model. However, the fact that the residual of the corresponding alignment of a spherical surface to a measured ideal spherical mirror is still around 3500 times smaller which means that either the ellipsoid is still not the best choice of a surface model or the positioning algorithm can still be improved.

When changing the surface model to the rotationally symmetric prolate ellipsoid, three new parameters have to be introduced to gain the fully model describing set of 7 parameters. A sphere is completely rotationally symmetric while a prolate ellipsoid is not. To the three spatial position parameters and the radius of a sphere two rotation parameters and a second radius have to be added in order to fully characterize the shape in space. These parameters have to be fixed during the fit of the surface model in the PMD evaluation process like described in chapter 2. The increased amount of free parameters might decrease the stability of the fit and the accuracy of the adjustment of the model during the evaluation. This issue should be examined in more detail in the future.

In conclusion, it can be said that the PMD evaluation of aspherical mirror facets using the assumption of an underlying rotationally symmetric prolate ellipsoidal surface model is a huge improvement compared to using a spherical surface model: the ellipsoidal surface model could be positioned much better than the spherical surface model and the curvature radii could be successfully reproduced compared to those obtained in previous measurements although this new approach is in a very early stage of development. Additionally only one measurement was needed instead of two compared to the previous chapters. For the future, more detailed studies of this new evaluation approach will help to better understand the issues with the ellipsoidal surface model and to further improve the measurement quality.

## 8 Summary and Outlook

The aim of this thesis is to adopt the existing mirror characterization and measurement procedures of spherical telescope mirrors to aspherical mirrors for the Schwarzschild–Couder telescope. This includes modifications to the existing evaluation approach as well as further development of the mirror characterization parameters. A new approach for evaluating aspherical mirrors is implemented and compared to the modified existing approach. It is made use of the mirror measuring technique *phase measuring deflectometry* (PMD, Wörnlein 2012), which is the approved method for measuring CTAs spherical telescope mirrors.

A short introduction to the principle of measuring mirrors with PMD was given in the first part of this thesis. The design concept of a Schwarzschild–Couder telescope for the medium sized telescopes for CTA was introduced and the mathematical surface definition of the mirrors of the primary dish was given. It was explained that single aspherical mirror facets like the P1 mirror were integrated in the simulation of PMD measurements in the form of meshes which consist of a set of triangles that approximate the ideal mirror surface. An adequate degree of discretization was determined with the help of ray tracing.

Subsequently simulated PMD measurements have been evaluated with the same approach used for spherical telescope mirrors discussed in chapter 2. The results obtained from this evaluation have been discussed. It was shown that a significant improvement of the measurement of aspherical mirrors can be achieved by measuring those in combination with a spherical reference mirror which is used to recalibrate the setup. In order to determine both curvature radii, aspherical mirrors have to be measured in two orientations. In this way the curvature radii of the aspherical mirror could be determined up to an accuracy of 0.5 %. The examined height deviation was shown to be affected by a systematics which was identified to be connected to the wrong assumption that the measured surface can be approximated by a perfect sphere. The related surface height deviation histogram is thus less conclusive. The corresponding mean value can be seen as a measure of fit quality which describes the degree of alignment of the measured surface and the describing model. The corresponding RMS value describes the surface deviation itself. In the future it can be used to characterize the quality of the surface of an aspherical mirror. Also the examined deviations of the slopes showed the observed problems in their determination. Nevertheless the slope deviation tendency graph offers a second possibility to state the aspherical mirrors quality.

The same analysis procedure was applied to the real aspherical mirror P1.016, a mirror element from the inner ring of the primary mirror dish which was built for a prototype SC MST. This mirror was measured also with the classical and well understood 2f method in order enable a classification of the results obtained with PMD. With the 2f measurement the sagittal curvature radius of this mirror was determined to be 0.23 % and the tangential

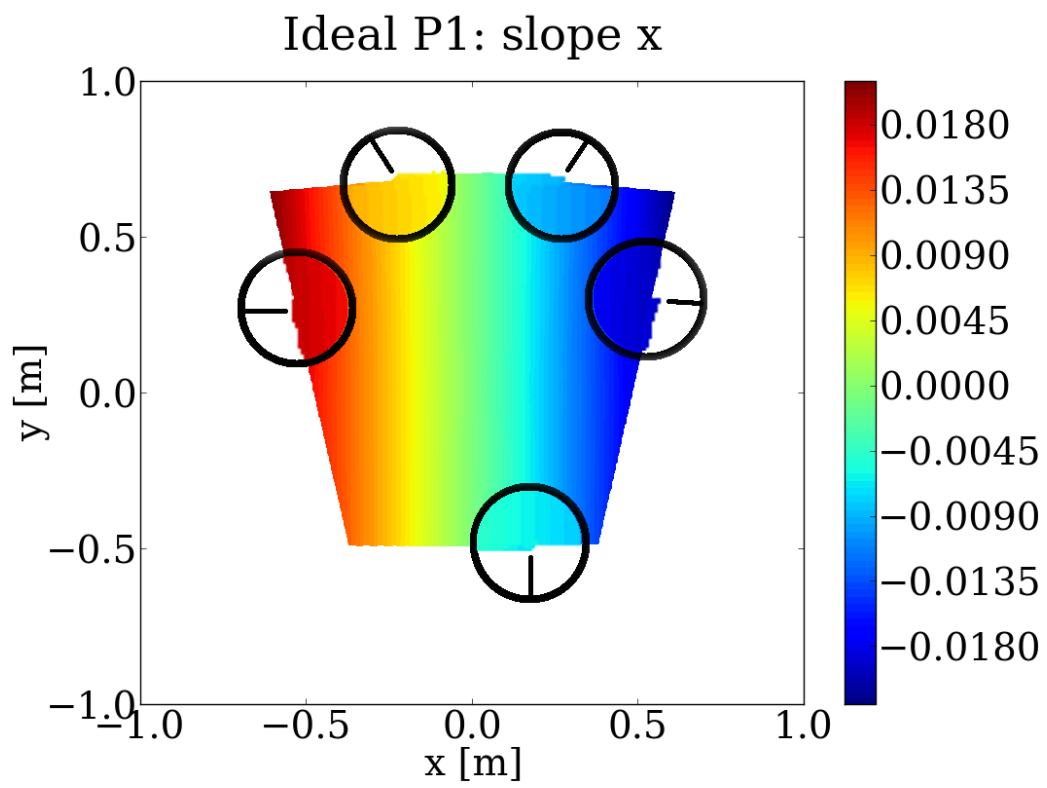


curvature radius 0.07 % smaller than the corresponding radii of the ideal mirror. The values obtained with the standard PMD evaluation show deviations of +1.10 % and +1.54 % relative to the 2f measurement. A distortion of the mirror surface in the middle of the mirror could be resolved in the evaluation procedure. The obtained surface deviation of the measured P1.016 mirror is around 17 % higher compared to the evaluated simulated mirror.

In the end a new evaluation approach was presented. In order to improve the surface model description, the assumption that the measured surface can be described approximately by an excerpt of a perfect sphere was abandoned and the model of a perfect rotationally symmetric prolate ellipsoid was introduced. The advantage of this shape is that it provides two curvature radii. The disadvantage is that the degree of freedom during the alignment fit rises compared to the fit of a spherical model which might result in a decreased stability and alignment capability. This new evaluation approach is at a very early stage of development and first results could be derived within this thesis. Test measurements with a simulated P1 mirror and the real P1.016 mirror showed that the determination of the curvature radii is possible from one single PMD measurement. Radii of an accuracy of +0.49 % and +0.48 % for sagittal and tangential curvatures can be obtained from the simulated data sets. Compared to the values obtained during the 2f measurement of the P1.016 mirror, the new PMD evaluation approach results in deviations of the curvature radii of +1.37 % and +0.21 % which are quantitatively comparable to those obtained with PMD earlier. Remarkable is the smaller residual remaining after the surface model fit in the PMD evaluation aligning the ellipsoidal surface model compared to aligning a spherical surface model and the smaller mean values of the surface deviation histograms. Also remarkable is the smaller RMS value of the surface deviation histogram for the measured ideal P1 mirror. The RMS value of the surface height deviation histogram for the measured P1.016 mirror is higher for the ellipsoidal evaluation approach than for the standard spherical approach. The reason for this observation and the origin of a systematics occurring in the slope determination process within the ellipsoidal evaluation approach are currently under investigation. These results indicate that the new ellipsoidal evaluation approach seems to be promising. Nevertheless, also the ellipsoidal surface model constitutes only an approximation of the exact surface structure of the aspherical mirror facets. For the future, more detailed studies need to be carried out in order to approve or abandon this approach.

Measuring single aspherical mirrors is a step that is needed in order to analyze the imaging quality of the full SC telescope optical system. Deviations of height and slopes can reveal surface coarseness and deviations of the curvature radii can give a measure of global deformations of a single mirror without the need of its counterpart. But keep in mind that the aim is to measure the amount of light that finally finishes up in one pixel of the telescope camera. At this stage of development this can hardly be stated by measuring just one single mirror facet. In which way characterizing measurement quantities of single mirrors describes the optical imaging properties of the entire telescope system will be the subject of future studies. The results of these studies will make it possible to develop constraints on those parameters which ensure a sufficiently good reflecting surface for the use in CTAs medium sized SCTs.

## Appendix



Larger image from figure 5.2. The data inside the markers is zoomed in.

## Bibliography

- Achary, B., Actis, M., Aghajani, T., et al. 2013, *Astroparticle Physics*, 43
- ATLAS Collaboration. 2012, *Physical Letters B*, 716, 1
- Bender, M. & Brill, M. 2006, *Computergrafik: Ein anwendungsorientiertes Lehrbuch*, Vol. 2 (Carl Hanser Verlag)
- Byrum, K. et al. 2015, A Medium Sized Schwarzschild-Couder Cherenkov Telescope Mechanical Design Proposed for the Cherenkov Telescope Array. (The 34th International Cosmic Ray Conference)
- Consortium, C. 2016, Official website of CTA, <https://portal.cta-observatory.org/Pages/Preparatory-Phase.aspx>
- Durham University. 2015, Ground Based Gamma Ray Astronomy, [www.dur.ac.uk/cfai/vhegammaraygroup/physics/groundbased/](http://www.dur.ac.uk/cfai/vhegammaraygroup/physics/groundbased/)
- Evans, L. & Bryant, P. 2008, *Journal of Instrumentation*, 3, 1
- Funk, S. 2015, *Annual Review of Nuclear and Particle Science*, 65, 245
- Gouraud, H. 1971, *IEEE Transactions on Computers*, C-20, pp. 623
- Häusler, G. 1999, Method and apparatus for determination of the shape or of the imaging properties of reflective or transparent objects, dE Patent App. DE1,999,144,354
- Helmholtz Association. 2016, Cosmic ray mystery, [www.hap-astroparticle.org/184.php](http://www.hap-astroparticle.org/184.php)
- Hinton, J., Sarkar, S., Torres, D., & Knapp, J. 2013, *Astroparticle Physics*, 43, 1
- Knauer, M. 2006, PhD thesis, University of Erlangen-Nuremberg
- Phong, B. 1975, *Communications of the ACM*, 18, 311
- Pickel, S. 2014, Simulation of a setup for phase measuring deflectometry (University of Erlangen-Nuremberg)
- Rousselle, J. & Vassiliev, V. 2013, Segmentation schemes for primary and secondary mirrors of the Schwarzschild-Couder telescope for CTA (CTA-US collaboration, MRI consortium, MLT Inc.)

- Schulz, A. 2010, PhD thesis, University of Erlangen-Nuremberg
- Schwarzschild, K. 1905, *Astronomische Mittheilungen der Königlichen Sternwarte zu Göttingen*
- UA1 Collaboration. 1983, *Physical Letters B*, 122, 103
- Vandenbroucke, J. 2014, in *Proceedings of Technology and Instrumentation in Particle Physics 2014 (TIPP2014)*. 2-6 June 2014. Amsterdam., 140
- Vassiliev, V. & Fegan, S. 2007, Schwarzschild-Couder two-mirror telescope for ground-based gamma-ray astronomy (30th international cosmic ray conference), arXiv:0708.2741
- Vassiliev, V., Fegan, S., & Brousseau, P. 2007, *Astroparticle Physics*, 28, 10, arXiv:astro-ph/0612718
- Vassiliev, V. & Rousselle, J. 2012, Optical System of 9.5m Schwarzschild-Couder Telescope for CTA (CTA-US Collaboration, MRI Consortium)
- Wenzel, J. 2014, Mitsuba Documentation, 0th edn. (Mitsuba)
- Wörnlein, A. 2012, Methods to measure optical properties of mirror facets for CTA (University of Erlangen-Nuremberg)

## Acknowledgment

I would like to thank everyone who has supported me during my master thesis. Special thanks to:

- Prof. Dr. Christopher van Eldik for giving me the opportunity to work on this interesting subject, for always taking time to discuss and for supervising my thesis.
- Prof. Dr. Gisela Anton for conceiving the second assessment.
- André Wörnlein for the great support and for his helpful comments.
- Alexander Ziegler for the nice and long revealing discussions.
- Domenico Tiziani, Giacomo Principe and Max Oberndörfer for making our office a place where effective work as well as enjoyable free time were possible.
- the whole group of CTA and H.E.S.S. for supporting my studies and for providing a pleasant working atmosphere.
- Monika Fink for her commitment and for making organizational matters as easy as possible.
- Patrick Hufschmidt, Tobias Ziegler, Katharina Witzmann, Reimund Bayerlein, Theresa Palm and Michael Wagenpfeil for providing relaxing moments in their offices.
- my family for supporting me during my thesis and for enabling my whole studies.

## Statement of authorship

I hereby certify that this thesis has been composed by me and is based on my own work, unless stated otherwise. No other person's work has been used without due acknowledgment in this thesis. All references and verbatim extracts have been quoted, and all sources of information, including graphs and data sets, have been specifically acknowledged.

Erlangen, November the 2nd, 2016

---

Andreas Specovius